Aalto University
School of Chemical
Engineering

Jarkko Etula

NOVEL IRON DOPED TETRAHEDRAL AMORPHOUS CARBON FILMS FOR ELECTROCHEMICAL DRUG SENSING APPLICATIONS

Master´s Programme in Chemical, Biochemical and Materials Engineering
Major in Functional Materials

Master's thesis for the degree of Master of Science in Technology
submitted for inspection, Espoo, 8 August, 2017.

Supervisor Professor Jari Koskinen

Instructor M.Sc. Niklas Wester

Aalto University
School of Chemical
Engineering

Aalto University, P.O. BOX 11000, 00076 AALTO
www.aalto.fi

Abstract of master's thesis

Author Jarkko Etula

Title of thesis Novel iron doped tetrahedral amorphous carbon films for electrochemical drug sensing applications

Degree Programme Master´s Programme in Chemical, Biochemical and Materials Engineering

Major Functional Materials

Thesis supervisor Prof. Jari Koskinen

Thesis advisor(s) / Thesis examiner(s) M.Sc. Niklas Wester

Date 08.08.2017 **Number of pages** 72 **Language** English

Abstract

The development of in vivo and in vitro methods for detection of neurotransmitters and active pharmaceutical ingredients, such as dopamine and paracetamol, is vital for the treatment of neurodegenerative disorders and drug overdosing. In this context, carbon nanostructures embedded with iron nanoparticles have been found to be desirable sensor materials in numerous cases. However, since complete removal of iron species from carbon nanostructures can be challenging, it is important to understand the specific electrochemical role iron species add to the carbon nanostructures. This effect was investigated in this work by controlled addition of iron into tetrahedral amorphous carbon (ta-C) thin films.

As of yet unreported iron doped ta-C (Fe/ta-C) thin films were fabricated with 2, 5 and 10 at% iron content using a room temperature filtered cathodic vacuum arc process. Deposited films were examined using extensive physical film characterization methods combined with electrochemical voltammetry and impedance techniques. Paracetamol and ascorbic acid were used as benchmark analytes. The addition of iron into ta-C films is found to 1) result in the embedding of non-oxidized iron nanocrystallites in the sp^3-rich carbon matrix, and 2) increase the selectivity and sensitivity of paracetamol detection by a cathodic shift of ascorbic acid oxidation potential. Furthermore, increased double-layer capacitance, enhanced electron transfer kinetics, dramatically lowered sheet resistance, and good electrochemical stability are achieved by the iron addition.

Compared to reference ta-C films, significant improvement in sensor performance is accomplished through iron doping. An important inference of this study is that iron species in carbon thin films are found to have an analyte-specific electrochemical role. This has far-reaching implications for the fabrication of tailored analyte-specific electrochemical thin film sensors. Furthermore, this suggests, that iron catalysts used in carbon nanostructure synthesis for sensing applications should be considered based on their application driven electrochemical role.

Keywords iron, nanoparticle, ta-C, DLC, composite, paracetamol, sensor, voltammetry

Tekijä Jarkko Etula

Työn nimi Rautaseostettu tetraedrinen amorfinen hiiliohutkalvo lääkeaineiden sähkökemialliseen havaitsemiseen

Koulutusohjelma Master´s Programme in Chemical, Biochemical and Materials Engineering

Pääaine Toiminnalliset materiaalit

Työn valvoja Prof. Jari Koskinen

Työn ohjaaja(t)/Työn tarkastaja(t) DI Niklas Wester

Päivämäärä 08.08.2017 **Sivumäärä** 72 **Kieli** Englanti

Tiivistelmä

Neurodegeneratiivisten häiriöiden ja lääkeaineyliannostusten hoitamista varten on tärkeää kehittää *in vivo* ja *in vitro* -menetelmiä hermovälittäjäaineiden ja lääkeaineiden kuten dopamiinin sekä parasetamolin havaitsemiseksi. Rautananopartikkeliseostetut hiilinanorakenteet ovat anturimateriaaleina hyvin soveltuvia näihin käyttötarkoituksiin. Koska rautayhdisteiden täydellinen poistaminen valmistetuista hiilinanorakenteista voi olla haastavaa, on tärkeää tutkia ja ymmärtää niitä sähkökemiallisia ominaisuuksia, joita raudan lisääminen tuo hiilinanorakenteisiin. Tässä työssä raudan lisäämisen vaikutusta tutkittiin lisäämällä sitä kontrolloidusti tetraedrisiin amorfisiin hiili-ohutkalvoihin (*engl*. tetrahedral amorphous carbon, ta-C).

Raudalla seostettuja ta-C-ohutkalvoja (Fe/ta-C) valmistettiin suodatettulla tyhjiökatodivalokaaripinnoitusprosessilla huoneenlämpötilassa 2, 5 ja 10 at%:n rautapitoisuudella. Valmistettuja kalvoja tutkittiin useilla fysikaalisilla karakterisointimenetelmillä sekä sähkökemiallisilla voltammetria- ja impedanssimittauksilla. Vertailuanalyytteinä sähkökemian mittauksissa käytettiin parasetamolia ja askorbiinihappoa. Raudan lisääminen ta-C-kalvoihin johti 1) raudan nanopartikkeleiden muodostumiseen sp^3-rikkaaseen hiilimatriisiin ja 2) parasetamolin havaitsemismittauksen selektiivisyyden ja herkkyyden kasvamiseen askorbiinihapon hapetuspotentiaalin pienentyessä. Lisäksi raudan lisääminen kasvatti ohutkalvon sähkökemiallista kaksikerroksista kapasitanssia, paransi elektronisiirron kinetiikkaa, madalsi merkittävästi pintaresistanssia, mutta ei heikentänyt sähkökemiallista stabiliteettia.

Raudan lisääminen ta-C-ohutkalvoihin parantaa merkittävästi anturin suorituskykyä mitatuilla vertailuanalyyteillä. Tämän tutkimuksen perusteella voidaan päätellä, että hiilirakenteisiin upotetuilla rautananopartikkeleilla on analyyttikohtainen sähkökemiallinen rooli. Tämä on tärkeä implikaatio, joka tulee ottaa huomioon sähkökemiallisten ohutkalvoantureiden valmistuksessa ja kehityksessä. Lisäksi on tärkeää huomioida, että hiilen nanorakenteiden synteesissä käytettävät rautakatalyytit kannattaa valita niiden sovelluslähtöisen sähkökemiallisen roolin perusteella.

Avainsanat rauta, nanopartikkeli, ta-C, DLC, komposiitti, parasetamoli, anturi, voltammetria

Acknowledgements

I want to thank my supervisor Prof. Jari Koskinen for his guidance and support during the process of developing and writing this Master´s Thesis. I am also grateful to my instructor M.Sc. Niklas Wester for his seemingly limitless insight, great feedback during proofreading, and scientific rigor in all matters encountered. Additionally, he conducted the electrochemical measurements of this study and showed me how to fabricate electrodes from the samples. During the long electrochemistry measurement nights, I always learned from him skills and knowledge far beyond the scope of the current work.

I would like to thank D.Sc. Ajai Iyer for the TEM work he performed for this study, his universal wisdom, and his strenuous efforts in proofreading. He is always the one to help with whatever problem, whether it be learning to use new equipment or trouble-shooting errors. He has also been the one in the first place to train me on SEM, Raman spectroscopy, and profilometry. I want to also thank B.Sc. Tom Lindqvist for maintaining and keeping the FCVA deposition system operational, and M.Sc. Jarmo Leppäniemi for his proofreading efforts.

I acknowledge funding from the Finnish Funding Agency for Innovation (Tekes) for the FEDOC-project (No. 211637), which focuses on developing a rapid and affordable method for opioid detection from blood samples. Also, the provision of facilities and technical support by Aalto University at OtaNano - Nanomicroscopy Center (Aalto-NMC) and RawMatTERS Finland Infrastructure (RAMI, No. 292884) is acknowledged.

Finally, I want to express my gratitude to my family and to my girlfriend Anna Kuukasjärvi for their love and support during the writing of this thesis.

Espoo, 8 August, 2017

Jarkko Etula

Table of Contents

Abbreviations

AA	Ascorbic acid
AC	Alternating current
a-C	Amorphous carbon, sp^2-rich
AFM	Atomic force microscopy
API	Active pharmaceutical ingredient
BDD	Boron doped diamond
CMOS	Complementary metal-oxide-semiconductor
CNT	Carbon nanotube
CV	Cyclic voltammetry
CVD	Chemical vapor deposition
DA	Dopamine
DC	Direct current
DI	Deionized water
DLC	Diamond-like carbon
DOS	Density of states
DPV	Differential pulse voltammetry
EDX	Energy-dispersive X-ray spectroscopy
EELS	Electron energy loss spectroscopy
EIS	Electrochemical impedance spectroscopy
Fe/ta-C	Iron doped tetrahedral amorphous carbon
FESEM	Field emission scanning electron microscopy
FFT	Fast Fourier transform
FWHM	Full width at half maximum
GIXRD	Grazing incidence X-ray diffraction
HRTEM	High-resolution transmission electron microscopy
PA	Paracetamol
PBS	Phosphate-buffered saline

PECVD	Plasma-enhanced chemical vapor deposition
p-FCVA	Pulsed filtered cathodic vacuum arc
PLD	Pulsed laser deposition
PTFE	Polytetrafluoroethylene
PVD	Physical vapor deposition
SAED	Selected area electron diffraction
SAXS	Small-angle X-ray scattering
SE	Secondary electron
SEM	Scanning electron microscopy
SERS	Surface-enhanced Raman spectroscopy
SHE	Standard hydrogen electrode
SIMS	Secondary ion mass spectroscopy
SPION	Superparamagnetic iron oxide nanoparticle
SWCNT	Single-walled carbon nanotube
ta-C	Tetrahedral amorphous carbon, $sp^3 > 60$ %
ta-C:H	Hydrogenated tetrahedral amorphous carbon
TEM	Transmission electron microscopy
UA	Uric acid
XAS	X-ray absorption spectroscopy
XPS	X-ray photoelectron spectroscopy
XRD	X-ray diffraction
XRF	X-ray fluorescence
XRR	X-ray reflectivity

1 Introduction

Novel iron nanoparticle catalysts have recently allowed several advancements in the field of electrocatalysis [1, 2], carbon nanotube and nanobud synthesis [3, 4], and electrochemical sensing of neurotransmitters [5, 6] as well as active pharmaceutical ingredients (API) [7]. Concurrently, there has been increased interest in *in vivo* and *in vitro* detection of neurotransmitters and APIs.

Paracetamol has been used as the benchmark analyte for API detection in publications based on graphene and carbon nanotube electrodes [8, 9]. In this biological context, relevant anti-oxidant interferants to be accounted for in analysis are ascorbic acid (AA) and uric acid (UA), which are present in high concentrations in biological samples [10]. Iron has a prominent catalytic role in these systems due to its commonness in biological functions [11-13]. Consequently, detection of paracetamol has been reported with an electrode comprising ferrocene thiolate stabilized iron oxides on gold particles with graphene [7].

In neurotransmitter detection applications, such as in the study of Parkinson's disease or other neurodegenerative disorders, a typical benchmark analyte is dopamine (DA) [14, 15]. Several iron containing carbon nanostructures and superparamagnetic iron oxide nanoparticles (SPIONs) have been effectively used in the detection of dopamine in the presence of interfering AA [6, 7, 16, 17].

In fuel-cell and electrolysis applications, iron and iron oxide containing nanostructures have a prominent position of interest compared to other catalytic nanomaterials due to their non-toxicity, biodegradability, low-cost, and availability [18]. In terms of performance, iron nanostructures on carbon platforms possess prominent catalytic effects in degradation/decomposition processes [18], and oxygen reduction reactions [19]. As an example, iron and iron oxide nanoparticles on graphene or single-walled carbon nanotube (SWCNT) [20-25] platforms have achieved notable performance advances compared to benchmark platinum catalysts [1]. Hence, iron and iron oxide containing carbon nanostructures, such as aerosol-synthesized carbon nanotubes, are highly versatile in electrocatalysis and sensing applications.

Nevertheless, to gain a fundamental understanding on the origins of this electrochemical behavior, iron nanostructures would have to be examined separately from the already active graphene and nanotube structures [26]. As detailed by Jurkschat et al. [26], it is understood that the iron oxide nanoparticles in carbon nanotubes are not removed even by super-washing in nitric acid [26]. In one solution, as proposed by Laurila et al. [27],

the catalytic nanoparticles embedded in the material should be considered as an essential part of the final structure, as per their desired electrochemical role. To investigate this idea without specifically attempting to remove iron from the original carbon material, such as SWCNT, iron is added into an initially relatively inert carbon platform. The carbon platform chosen is tetrahedral amorphous carbon (ta-C). Due to its high fraction of sp^3-bonded carbon, pure ta-C is chemically reasonably inert, mechanically resilient, biocompatible, has a wide water window, and is resistant against passivation by proteins [28-31]. Also, facile outer sphere electron transfer has been achieved for ultrathin ta-C electrodes [31]. Such properties make pure ta-C thin film electrodes suitable for applications in biological and electrochemical sensing.

In the context of *in vitro* API detection, this study investigates the electrical and electrochemical benefits induced by the addition of iron into ta-C films, hereby known as Fe/ta-C. Paracetamol is selected as the API analyte to be investigated. Also, the common interferant ascorbic acid is studied. Improvements are expected in enhanced electron transfer kinetics, while preserving the favorable properties of ta-C, such as its wide water window [28, 32].

The Fe/ta-C films are characterized by X-ray reflectivity (XRR), grazing incidence X-ray diffraction (GIXRD), scanning electron microscopy (SEM), energy-dispersive X-ray spectroscopy (EDX), atomic force microscopy (AFM), transmission electron microscopy (TEM), select area electron diffraction (SAED), Raman spectroscopy, and four point probe. These results are then utilized to explain the electrochemical characteristics obtained from cyclic voltammetry (CV) measurements. Measurements are carried out with sulfuric acid, ascorbic acid, paracetamol and hexaammineruthenium. Electrochemical impedance spectroscopy (EIS) in hexaammineruthenium is also performed to further investigate the electron transfer kinetics.

2 Tetrahedral Amorphous Carbon

Tetrahedral amorphous carbon, or ta-C, is a type of diamond-like carbon (DLC) thin film, which has sp^3-fraction of at least 60 %, and minimal impurities. In this work, ta-C and Fe/ta-C films are deposited using a physical vapor deposition (PVD) method called pulsed filtered cathodic vacuum arc (p-FCVA). The reader is requested to refer the review by Robertson [30] for exhaustive details on DLC characterization and deposition methods, as well as properties.

As illustrated in the ternary phase diagram for amorphous carbon and hydrogen in Figure 1, there are only small amounts of hydrogen present in ta-C films. It should be noted, that in addition to p-FCVA, ta-C can also be deposited using other common PVD and CVD methods, such as pulsed laser deposition (PLD) or plasma enhanced chemical vapor deposition (PECVD). In case of CVD, hydrogenated ta-C:H films are deposited, since the used precursors contain hydrogen. [30]

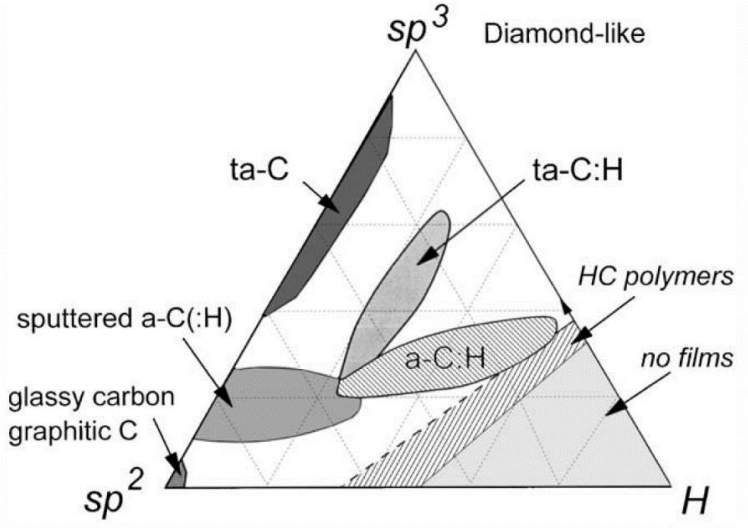

Figure 1. Ternary phase diagram of amorphous carbon for sp^2 and sp^3-bonding, as well as hydrogen content. Reprinted from J. Robertson [30].

As explained by Robertson [30], models of ta-C structure describe it as a dielectric, comprising random networks of sp^2 and sp^3 hybridized carbon atoms. According to refined models, the structure is controlled by the π-bonding of the sp^2-sites. The sp^2-sites favor clustering to maximize their π-bonding energy, and if the fraction of sp^2 increases, this process yields planar aromatic sites that eventually form graphitic clusters. In general, the conductivity of ta-C films can be determined by the relative separation of these low resistance, small band gap sp^2-clusters separated by large band gap sp^3-sites. When deposited using high-energy C^+ ion processes, such as FCVA or PLD, the surface interface

layer of ta-C has a higher sp^2-fraction compared to its bulk, and can be described as being similar to amorphous carbon, or a-C [33, 34]. Compared to bulk ta-C, this high sp^2-fraction surface exhibits a different band gap structure as shown in literature [32, 34].

In the case of added iron, the additional Fe atoms are expected to enhance conductivity by increasing density of states (DOS). It is common to tailor the ta-C properties by the addition of dopants, such as nitrogen for increased conductivity [35], tungsten for a lower friction coefficient [36], or nanodiamonds for improved hardness and wear resistance [37].

The p-FCVA deposition method for ta-C has several advantageous features towards bio-sensing applications as described in literature [30]. First, it is a room temperature process, which makes it fully compatible with CMOS and other low-thermal-budget technologies. Second, it is adaptable to standard silicon processes and is patternable. Third, due to the high vacuum during deposition, there is negligible amount of oxygen, water or other gases and contaminants. Finally, multiple cathode material arrangements allow simultaneous co-deposition and doping of the films with any relatively conductive target material, or process gas. A disadvantage of cathodic arc processes is the release of macroparticles from the target material. This downside can be diminished at the cost of deposition rate using electromagnetic lenses, such as the 45 degree single-bend plasma filter used in this study shown in Figure 2 attached to the p-FCVA cathode-anode assembly.

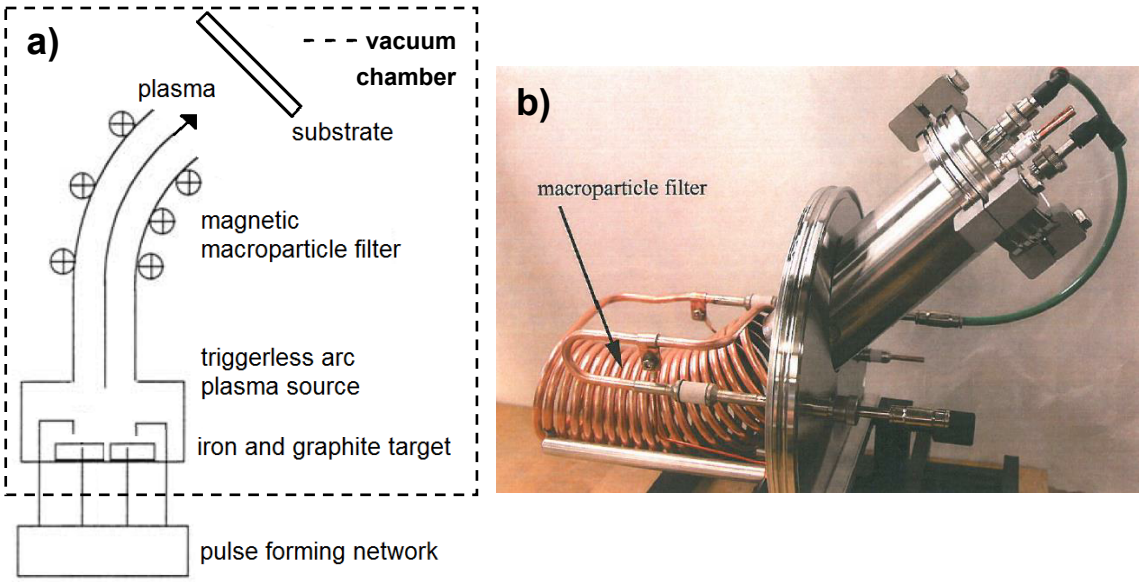

Figure 2. The single-bend p-FCVA cathode-anode assembly used in this work. a) A schematic indicating relevant components and the 45 degree geometry, modified from J. Robertson [30]. b) Picture of the cathode-anode assembly, as removed from the vacuum chamber.

3 Voltammetry

When discussing biological or industrial electrochemical applications of electrode materials, the concept of water window, or electrochemical window in aqueous solution, is important. Specific to each electrode material, it can be described as the potential range and difference between the reduction and oxidation potentials of water [38]. For example in the case of electrocatalysis of water, the water window for a certain electrode material is engineered to be as small as feasibly possible to reduce the overpotential required for evolution of oxygen or hydrogen. On the contrary, in the case of detection of a chosen analyte in biological systems, the water window is tailored to be wide enough to accommodate the potential range required for detecting the analyte. As required by some biosensing electrode applications, ta-C films are known to have a wide water window, low capacitive background current, and relatively high chemical inertness [32].

Cyclic voltammetry is an effective and versatile tool in electrochemical detection of electroactive analytes such as neurotransmitters and APIs due to its good temporal and spatial resolution. In the three-electrode cyclic voltammetry setup, the potential of the working electrode is swept linearly with respect to reference and counter electrode, with scan rate (υ), from initial potential (E_i) to switching potential (E_λ), and back. The resulting current during the voltage sweep is recorded, and the number of cycles studied can be varied. As illustrated in Figure 3, oxidation and reduction reactions are observed as peaks of positive and negative currents respectively. Initially, the potential is increased from E_i, and when the oxidation potential is reached, oxidation of analyte begins. This causes depletion of analyte from the electrode surface resulting in a concentration gradient, inducing mass transfer. The maximum rate of mass transfer during oxidation, corresponding to $I_{p\ ox}$, is reached at the peak potential ($E_{p\ ox}$). After E_λ, and given the reaction is reversible, the reverse scan similarly reduces the previously oxidized species. [38]

Figure 3 is an example voltammogram for a fully reversible outer sphere redox reaction. The figure shows how to calculate background subtraction (dashed lines), and obtain electrochemical parameters, such as oxidation and reduction peak current ratio ($I_{p\ ox}/I_{p\ red}$), and the redox peak potential separation (ΔE_p). As described by Nicholson [39] and Bard [38], for a redox reaction to be reversible, $I_{p\ ox}/I_{p\ red}$ has to be close to unity, and ΔE_p be about 60 mV/n, where n is the number of electrons transferred.

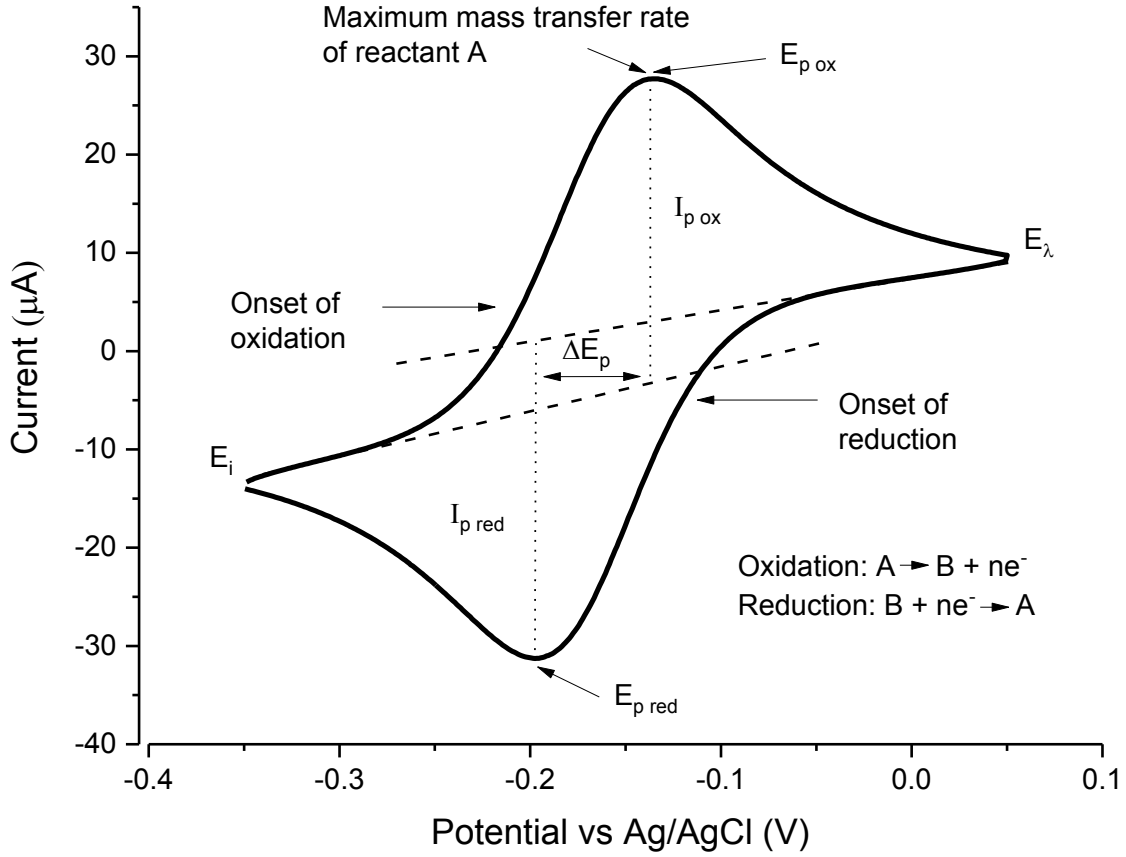

Figure 3. Example of a fully reversible cyclic voltammogram for an outer sphere redox reaction. Dashed lines show background subtractions, which can be used to calculate the oxidation and reduction peak current ratio $I_{p\,ox}/I_{p\,red}$, and the peak potential separation ΔE_p.

The so called faradaic current (i) is electron transfer between the working electrode and the analyte, and can be related to the selected scan rate (υ), electrode area (A) and the total charge transferred (nF) in the reaction [38]. Equation 1 is used to describe this as:

$$i = nFA\upsilon \tag{1}$$

Depending on the species and electrodes studied, high scan rates may give rise to detrimental effects from double-layer capacitance (charging currents) and uncompensated resistance, also known as iR_u drop. The first of the two, charging current (i_c), is a non-faradaic process where no electron transfer takes place, but the electrical double-layer on the electrode surface collects charge according to Equation 2:

$$|i_c| = AC_{dl}\upsilon, \tag{2}$$

where A is the electrode area, C_{dl} is the double-layer capacitance and υ is the scan rate [38]. In CV experiments, the potential sweep may also cause faradaic reactions to

occur on the electrode surface. The current arising from the surface faradaic redox reactions and capacitive current is called pseudo-capacitive current, and can be measured with CV. Equation 2 can be used to experimentally determine the pseudo-capacitance of a reaction from a cyclic voltammogram by plotting i_c as a function of several scanning speeds giving C_{dl} as the slope. It should be noted, that if the double-layer capacitance and uncompensated resistance are large, this method to determine C_{dl} experimentally can be unreliable. More reliable and accurate double-layer capacitance values can be obtained from electrochemical impedance spectroscopy (EIS). To improve the pseudo-capacitance measurement, the capacitive current can be measured from potential ranges where no assumed faradaic electron transfer is taking place. [38]

The uncompensated resistance (R_u) arises from the resistive nature of the electrolyte and electrode used. Solution resistance and intrinsic resistance of the electrode together yield the uncompensated resistance, which causes an ohmic drop (iR_u) to the total potential $E + iR_u$ being measured [38]. The effect of iR_u increases as a function of peak current measured and low iR_u can be reliably compensated with modern potentiostats, such as the Gamry Reference 600 used in this study. Nevertheless, R_u values should always be measured in preliminary testing to detect faults in electrode fabrication.

4 Experimental

In section 4.1, the thin film deposition system used and its respective calibration for Fe and ta-C is described with subsequent Fe/ta-C composite deposition. Then, section 4.2 describes characterization methods utilized to study the deposited composite films.

4.1 Film Deposition and Calibration

Fe, ta-C, and Fe/ta-C films were deposited with a pulsed filtered cathodic vacuum arc system (p-FCVA). The Kurt J. Lesker Company vacuum system consists of an Edwards XDS 10 roughing pump and a CTI cryogenics CTI 8F cryopump. The vacuum chamber was evacuated to pressures below $5 \cdot 10^{-7}$ Torr prior to deposition. The p-FCVA system uses a toroidal 45 degree bent electromagnetic filter, with a single pulse forming network unit of 2.6 mF charged to -400 V (pulse current 650 A) to initiate a triggerless arc between the cathode and the surrounding anode body. The cathode assembly consists of two separate cathodes of different materials, carbon and iron, surrounded by a shared anode body. A self-designed Labview based software running on National Instruments hardware controls the triggering of the pulse-forming network with a frequency of 1.0 Hz and triggers one cathode after the other as defined by the chosen pulse ratios.

The substrates, placed 110 mm away from the end of filter coil, were at floating potential and room temperature. The substrate holder was rotated at 17 rpm to ensure uniform film thickness. The source material for carbon plasma is a graphite rod of 6.35 mm diameter and purity of 99.95 % (Graphitestore). The source material for iron plasma is an iron rod of similar diameter and purity 99.99 % (Goodfellow).

4.1.1 Substrate Preparation

Boron doped p-type silicon (100) prime wafers (< 0.005 Ωcm, Siegert Wafer), microscope glass slides (Menzel), and NaCl single crystals (TedPella), were used as substrates. Silicon wafers and glass slides were first cleaved into smaller pieces of 20x20 mm, then cleaned ultrasonically in high purity liquid chromatography grade acetone (Sigma Aldrich), and finally dried with lens paper (Kodak) in slow methodical swiping motions towards the edge of the piece.

For planar TEM and SAED imaging, the film deposited on the salt crystals was prepared into a TEM compatible specimen by floating off the film on top of DI water surface. The salt crystal was gently inserted into the DI water bath at a shallow angle. A suitably small piece of film was broken off and fished onto an M75 copper-only TEM grid (Agar).

Before inserting the specimen holder into TEM, the samples were heated on a hotplate at 60°C for 10 minutes to remove excess water. For profilometry measurements, one Si-piece in each deposition was marked with a cross using a polymer marker. This polymer was later removed by lift-off in acetone to create trenches.

4.1.2 Deposition Rate Calibration

As shown by Kohli et al. [40], X-ray reflectivity (XRR) is a reliable thickness evaluation tool, when supported by additional thickness verification methods. In this work, calibration of the p-FCVA sources for iron and carbon, was carried out using XRR, supported by contact profilometry. First, single element films of C and Fe were deposited for thicknesses corresponding to 400, 600, as well as 800 pulses, and measured by XRR. The deposition rates were measured to be 0.0863 nm/pulse for ta-C, and 0.0331 nm/pulse for Fe. Tables of calibration samples, X-ray reflectivity results, and calculated deposition rate values can be found in Appendix A. Deposition rates were calculated as linear functions, even though the deposition rate per pulse decreases slightly as the cathode material erodes. Consequently, all films in this study were deposited from freshly maintained and pre-cleaned cathode sources.

The molar deposition rates of carbon and iron (mol/(pulse$\cdot$area)) can be calculated using the following factors: molar masses (g/mol), deposition rates (nm/pulse), and XRR film density (g/cm^3). Then, for a mixed dual-cathode deposition of Fe and C to form Fe/ta-C, the expected number of pulses for desired Fe at% can be calculated. Based on previous studies of metal doped DLC [41-46], Fe atomic percentages of 2, 5, and 10 at% were chosen for this work. Based on calibration data, these Fe at% values correspond to p-FCVA cathode pulse ratios of 1:10, 1:4, and 1:2 (Fe:C). For all the pulse ratios, it must be noted, that the carbon cathode is selected to trigger last, depositing a thin layer of carbon as the final layer. The thickness of Fe/ta-C and reference ta-C films for this study was chosen to be 30 nm. In this work, Fe atomic percentage in Fe/ta-C is selected as the independent variable. Hence, any investigated dependent variable, such as film roughness or sheet resistance, is plotted as a function of Fe at%.

4.2 Characterization Methods

The following subsections describe the characterization methods used to study the deposited films, as explained in the previous section.

4.2.1 X-ray Reflectivity and Diffraction

Grazing incidence X-ray diffraction (GIXRD) and XRR measurements were performed using a Rigaku SmartLab diffractometer equipped with a 9 kW rotating Cu anode (0.154 nm wavelength) and HyPix-3000 2D single photon counting detector operated in 1D mode. All measurements were conducted in parallel beam mode with an incidence $K_{\alpha 1}$ monochromator, a 5 mm horizontal slit, and 5 deg angular aperture Soller slits at both incident and detector ends.

For XRR measurements, an incidence vertical limiting slit of 0.150 mm was used and the measured reflectivity spectra was normalized and fitted using Rigaku GlobalFit software for film parameters, as per Parratt formalism [47-49]. The XRR scans were performed in the range of 0-5 degrees 2-theta, scan rate of 0.4084 deg/min, and step size of 0.0002 deg. For ease of viewing, the XRR 2-theta data were smoothed to a step size of 0.001 deg using adjacent-averaging. For GIXRD measurements, the incident vertical slit was varied depending on the investigated incident omega (ω) angle, determined from XRR profiles. In order to maximize interaction evanescent wave area, and avoid beam spillage and noise, the total longitudinal footprint of incident beam dependent on ω and vertical limiting slit was restricted. GIXRD scans were performed in the range of 25-93 degrees 2-theta, with a scan rate of 1.00 deg/min, and a step size of 0.02 deg. Known GIXRD silicon background peaks (311) were removed as per literature [50-53].

XRR simulations were fitted systematically on a silicon base-layer of density 2.33 g/cm^3 according to the following principles: each sample was assumed to have an SiO_2 layer of fixed density 2.2 g/cm^3, thickness of less than 2 nm, and a root mean squared surface roughness (R_q) of less than 0.5 nm [54]. As for the calibration ta-C films, according to work by Robertson & Ferrari [30, 55] there exists a surface layer of amorphous carbon of lower density. For simplicity, we disregard this notion in this work and it is deemed feasible for the XRR simulations to approximate parameters for a single and uniform ta-C layer. Maximum density of each layer was restricted to the typical density of the heaviest element present in the layer, such as iron 7.87 g/cm^3 or ta-C 3.20 g/cm^3 [55].

For the iron thin films, the XRR simulation and corresponding Extended Fourier Analysis suggested electron density contrast i.e. inhomogeneity throughout the deposited iron

films. Similar XRR work by Solina et al. proposed the addition of oxide layers to the bottom and top of metal thin films [56]. Therefore, three iron layers of different densities were simulated to match the experimental data. The rough surface layer, likely exposed to atmospheric moisture and oxidation, has a lower density. The middle layer, with practically zero roughness to its surrounding iron matrix, exhibits density identical to bulk iron. The bottom layer, with proximity to the substrate, has again lower density and increased roughness. No further assumptions were introduced due to limited knowledge about the films.

4.2.2 Scanning Electron Microscopy

Cross-sectional FESEM analysis of the samples was performed by a Hitachi S-4700 SEM at 30 kV accelerating voltage using secondary electron (SE) detectors. The samples were prepared by wafer cleaving techniques and mounted on a 90 deg aluminum cross section holder. Two images with a magnification of 200k were taken from each sample and the thickness measured from three places in each image using ImageJ image processing software. These values were used to calculate the average thickness and standard deviation for each sample.

Energy-dispersive X-ray (EDX) spectra of iron were also acquired using Oxford Instruments INCA X-Sight 7200. In this work, the EDX was utilized in a semi-quantitative manner to observe relative Fe content differences between the investigated samples. To enable this relative comparison, Fe K_α peak intensity in EDX spectrum for each measurement was normalized to the intensity of the silicon substrate. Three measurements were performed for each sample and averaged with standard deviation as the error margin. Similar semi-quantitative EDX methods have been conducted e.g. by Matsutani et al. [57].

4.2.3 Profilometry

Contact profilometry thickness measurements were carried out using Dektak 6M profilometer. For each sample, three 800 μm long thickness profiles were scanned across the trenches formed by marker lift-off. The profiles were analyzed and averaged with standard deviation of the population used to represent the experimental error margins.

4.2.4 Atomic Force Microscopy

A Veeco Dimension 5000 AFM was used in tapping mode. Mikromasch HQ:NSC14/Al BS tips of 8 nm typical tip radius and 5 N/m force constant were used. For each sample,

initial scans of 5x5 μm (512x512 point resolution) were used to find 1x1 μm (2048x2048) areas free of large particles. These 1x1 μm areas were mapped to compute the root mean squared surface roughness (R_q). Data was collected for height, amplitude error, and phase. Supported by literature [44, 58, 59], images were processed using Gwyddion 2.47 software for artifact correction by matching the alignment of subsequent rows, vertical 1st order background subtraction, and correction of horizontal strokes.

4.2.5 Transmission Electron Microscopy

TEM analysis was performed by a FEI Tecnai F-20 TEM at 200 kV acceleration voltage, operating on sensitive beam settings. Select area electron diffraction (SAED) and TEM micrographs were obtained for Fe/ta-C samples of 2, 5, and 10 at% Fe. The acquired images were processed on Gatan DigitalMicrograph and ImageJ. For comparative analysis of TEM micrographs and SAED diffractograms, fast Fourier transforms (FFT) of micrographs were computed to highlight Fe lattice spacings. For verification of Fe crystal structure, SAED diffractograms were processed and simulated into suitable 2-theta diffractograms, which were then inserted into PANalytical Highscore Plus, where respective diffraction lattices and elemental phases were identified. No TEM-based crystallographic analysis was performed for ta-C as it is amorphous.

4.2.6 Four Point Probe

Four point probe measurements were carried out for glass substrate samples on a Hewlett-Packard 3458A multimeter, attached to a Jandel RM3000 multi height probe. For each sample, average sheet resistance and standard deviation values were calculated from six measurements.

4.2.7 Raman Spectroscopy

Raman spectroscopy was performed by a Horiba Jobin-Yvon Labram HR confocal Raman system with an argon laser of 488 nm wavelength and 10 mW power on sample. Spot size of 1 μm was used with an Olympus 100x objective. Raman spectra were acquired in the range of 50 to 3000 cm^{-1} with a 600 lines/inch diffraction grating, exposure time of 15 s, and accumulation averaging count of two. Spectroscopic calibration was performed using an intrinsic Si wafer (Ultrasil) and adjusting the silicon peak FWHM value to 520.0 cm^{-1}. Raman spectra were obtained from three well separated places and fitted by two Gaussian peaks for D and G regions of amorphous carbon, as explained in literature [60]. For each sample, the acquired spectra were fitted independently to compute the average and standard deviation values, as well as the I(D)/I(G) peak intensity ratios.

4.3 Electrochemical Characterization

All electrochemical measurements were carried out on Gamry Reference 600 potentiostat and analysed using Gamry Echem Analyst software. Both CV and EIS measurements were carried out in a three-electrode cell with an Ag/AgCl (+0.199 V vs. SHE, Radiometer Analytical) reference electrode and a platinum wire counter electrode. Aqueous solutions of 1 M KCl and phosphate buffered saline solution (PBS, pH 7.4) were made from distilled water, and were de-aerated for at least 15 minutes with N_2(g) before measurements. In addition, during the measurements the cell was blanketed in a continuous flow of nitrogen. Before all measurement sets, preliminary scans were used to determine the appropriate potential windows for the unknown samples, supported by previous publications of similar electrode materials [61, 62]. All electrodes were prepared by masking the samples with PTFE tape (Irpola) onto FR-4 copper laminate sheets (MG Chemicals). Electrode preparation quality was evaluated using preliminary uncompensated resistance R_u approximations in the supporting electrolyte intended for measurement to discard electrodes of $R_u > 80\ \Omega$. Hence, when measuring low currents of around 10 μA, the ohmic drop resulting from R_u is only a few millivolts and can be disregarded.

4.3.1 Cyclic Voltammetry

For all cyclic voltammetry measurements, the following data were analyzed using Gamry Echem Analyst: oxidation and reduction peak currents (I_p), potentials (E_p), peak potential separation (ΔE_p), peak current ratios ($I_{p\ ox}/I_{p\ red}$), and respective background corrections. Where appropriate, currents and capacitances were normalized to the active electrode surface area of 3 mm diameter equating to an area of 0.07069 cm^2.

The potential window, also known as water window, was determined for the investigated samples in 0.15 M H_2SO_4 (Merck Suprapur) by cycling the samples at a scan rate of 400 mV/s until a steady state was achieved and the absolute value of current was about 200 μA for both anodic and cathodic side. Capacitive currents and the pseudo-capacitance were also determined from the average background currents (between -50 and +50 mV) around zero potential, for anodic and cathodic segments, at 50 and 400 mV/s scan rates. The applied potential window for capacitive current measurements was -200 to +200 mV. As previously described by Equation 2 in section 2, the pseudo-capacitance can be determined as the slope of capacitive current vs. scan rate. To investigate the effect of Fe at% on electrochemical activity of ascorbic acid (Sigma-Aldrich) and paracetamol (Sigma-Aldrich), cyclic voltammetry studies were

conducted separately for 1 mM ascorbic acid and 1 mM paracetamol, both in PBS. Scan rates of 10, 25, 50, 100, 200, 300, 400, 500, 750, and 1000 mV/s were measured, and respective oxidation/reduction peak potentials determined. To determine whether the electrochemical systems were diffusion limited, oxidation peak currents were plotted as a function of square root of scan rate ($\upsilon^{1/2}$) [38, 63].

To investigate the sample electron transfer kinetics independent from the surface chemistry [64], cyclic voltammetry measurements in 1 mM $Ru(NH_3)_6$ (Sigma-Aldrich) dissolved in 1 M KCl (Sigma Aldrich) were performed at scanning rates of 10, 25, 50, 100, 200, 300, 400, 500, 750, and 1000 mV/s.

4.3.2 Electrochemical Impedance Spectroscopy

EIS measurements were conducted in 5 mM $Ru(NH_3)_6$ dissolved in 1 M KCl to investigate the effect of added iron on film charge transfer resistance (R_{ct}) and double-layer capacitance (C_{dl}). An AC signal of 15 mV amplitude was used in the frequency range from 200 kHz to 100 mHz. CV measurements at 400 mV/s were used to determine the formal potentials of the $Ru(NH_3)_6^{3+/2+}$ redox system, which were set as the DC potentials for EIS.

Obtained EIS spectra were fitted and analyzed using Gamry Echem Analyst software. The equivalent circuit used for fitting the Nyquist plots was a modified Randles circuit with a solution resistance (R_s) in series with parallel circuit of a charge transfer resistance (R_{ct}), a Warburg element, and a constant phase element for the double-layer capacitance (C_{dl}). The R_{ct} element comprises of two resistance elements: electron transfer to the film surface, and electron transfer through the film. For the C_{dl}, ideal capacitor parameter ($a = 1$ for ideal capacitor), and apparent heterogeneous rate constant (k^0_{app}), were calculated as described by Hsu & Mansfeld [65].

5 Results

5.1 Film Characteristics

5.1.1 Thickness

X-ray reflectivity (XRR) results are displayed in Figure 4 in the range of 0 to 5 degrees 2-theta with experimental data in red and simulated data in blue. The calculated XRR thickness, density, and roughness values are tabulated in Table 1. With increased Fe at%, the XRR signal intensity decreased below appreciable counts beyond 4 degrees 2-theta.

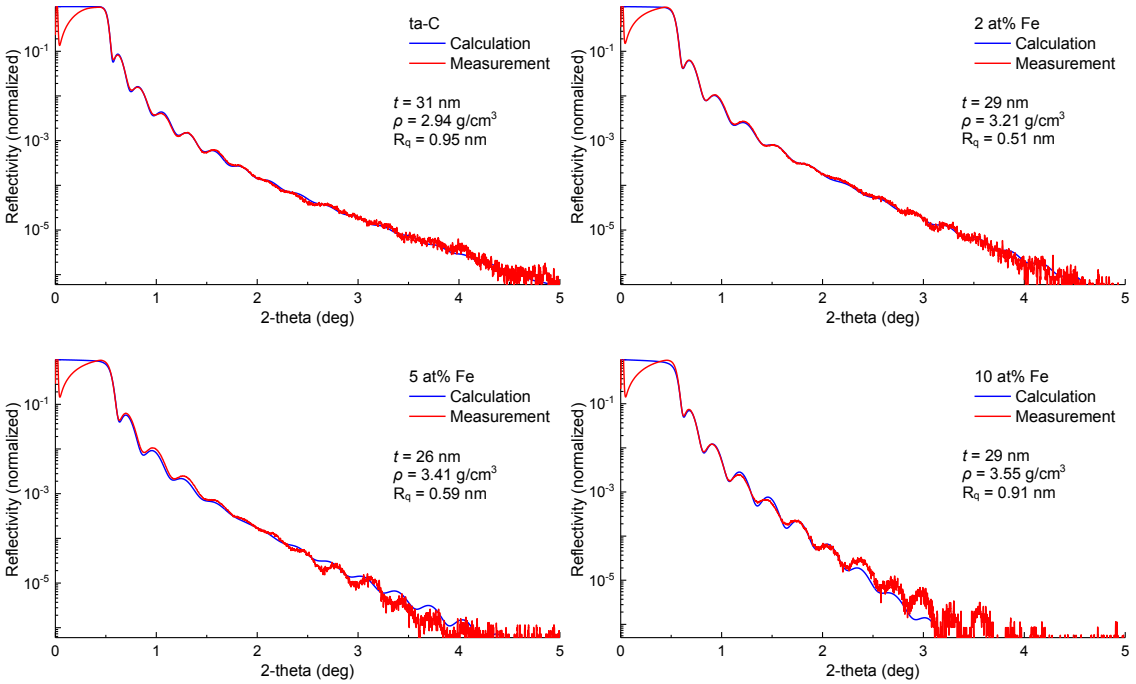

Figure 4. Measured X-ray reflectivity scans showing experimental and simulation data in red and blue, respectively. Calculated density (ρ), and roughness (R_q) were found to increase as a function of Fe at%, whereas thickness (t) remained similar.

The XRR experimental and simulation results in Figure 4 are in good agreement for all samples and the calculated values are also in agreement with supporting FESEM and profilometry thickness values in Table 1. The results show a consistent increase in density as a function of Fe at%, seen as an increased critical angle in Figure 4. Also, the film roughness in XRR simulation for the Fe/ta-C samples appears to increase with added iron. Although all samples are of comparable thickness, slight variations are expected with the p-FCVA process. Appendix A exhibits additional XRR results with complete

descriptions of simulated film parameters and comparisons between expected and measured film density profiles.

Field emission scanning electron microscopy (FESEM) cross-section images are displayed in Figure 5 and the corresponding thickness values tabulated in Table 1 on the next page. No visible distinctions could be made between the samples since all showed ultra-smooth surface roughness, similar cross-section structure, and similar thickness.

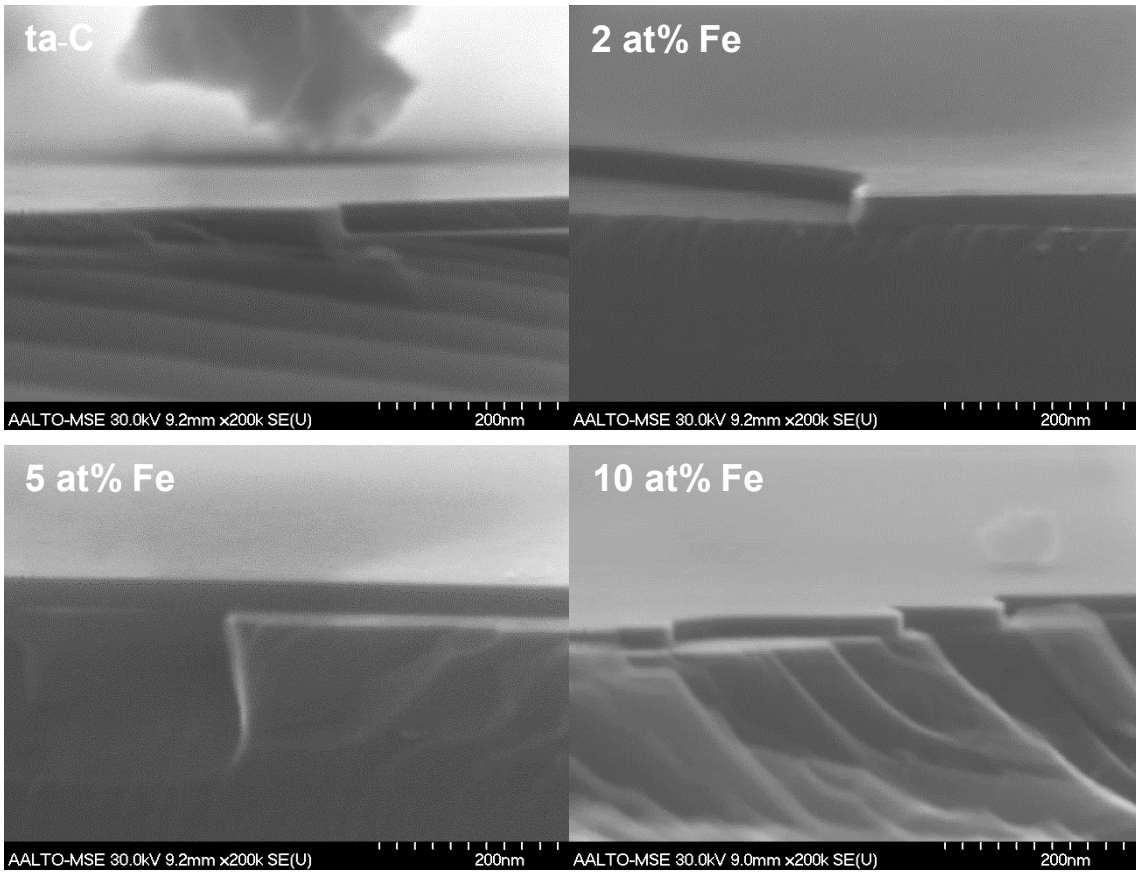

Figure 5. FESEM cross-section images of investigated samples in magnification of 200k.

The thickness measured by XRR, FESEM, and profilometry as a function of Fe at% with standard deviations as error bars are summarized in Figure 6. The thickness measured for all samples by different methods is in good agreement within experimental errors.

Table 1. Summary of measured thickness and standard deviation values (in parentheses) obtained by XRR, profilometry and FESEM cross-section. The expected thickness values correspond to deposition rates calibrations. Additional XRR roughness and density results are also displayed.

Method	ta-C	2 at% Fe	5 at% Fe	10 at% Fe
Expected thickness (nm)	30	30	30	30
XRR Thickness (nm)	31	29	26	29
Profilometry Thickness (nm)	27 (5)	27 (5)	27 (2)	28 (4)
FESEM Cross-section (nm)	33 (1)	26 (1)	25 (2)	26 (1)
XRR Density (g/cm^3)	2.94	3.21	3.41	3.55
XRR Roughness (nm)	0.95	0.51	0.59	0.91

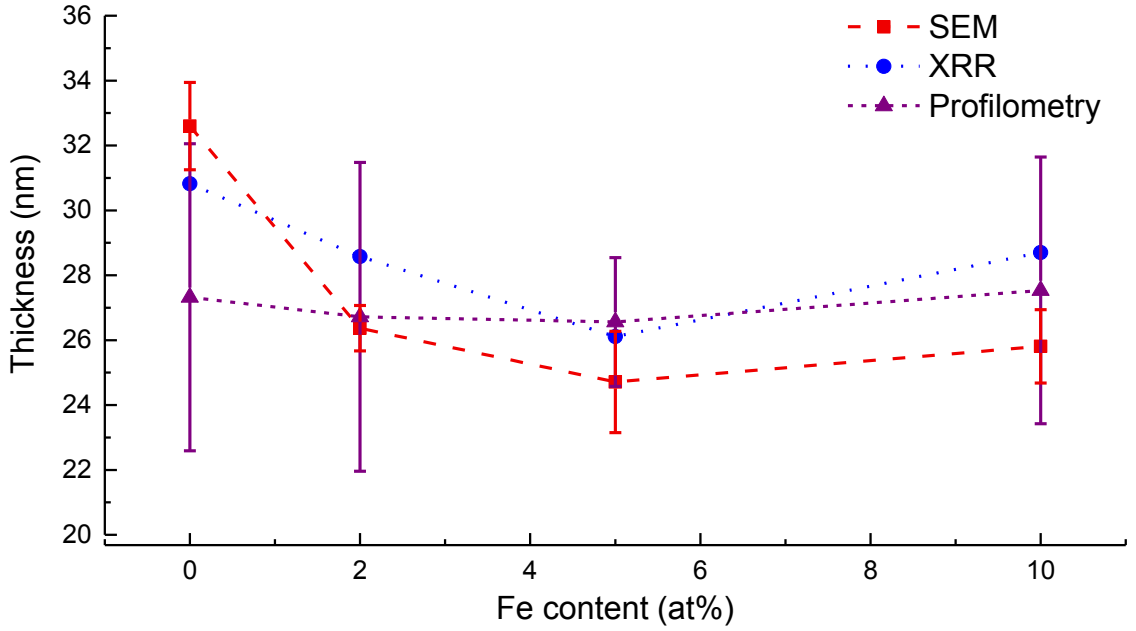

Figure 6. Summary of measured thicknesses in nanometers with standard deviations as error bars. These results point to all samples being of similar thickness within experimental error.

5.1.2 Roughness

X-ray reflectivity and atomic force microscopy (AFM) topography measurements were utilized to investigate the sample roughness as a function of Fe at%. AFM topography scans of 1 μm areas are shown in Figure 7. Although the root mean squared (R_q) roughness values calculated from Figure 7 are practically identical between the samples,

a slight surface undulation is observed in the micrometer scale for the 10 at% Fe sample. This unique surface topography was also observed in the optical microscopes of AFM and Raman (not shown). Appendix B further demonstrates this topography on larger scales by including the 5x5 μm AFM images that were used to select the 1x1 μm areas shown in Figure 7.

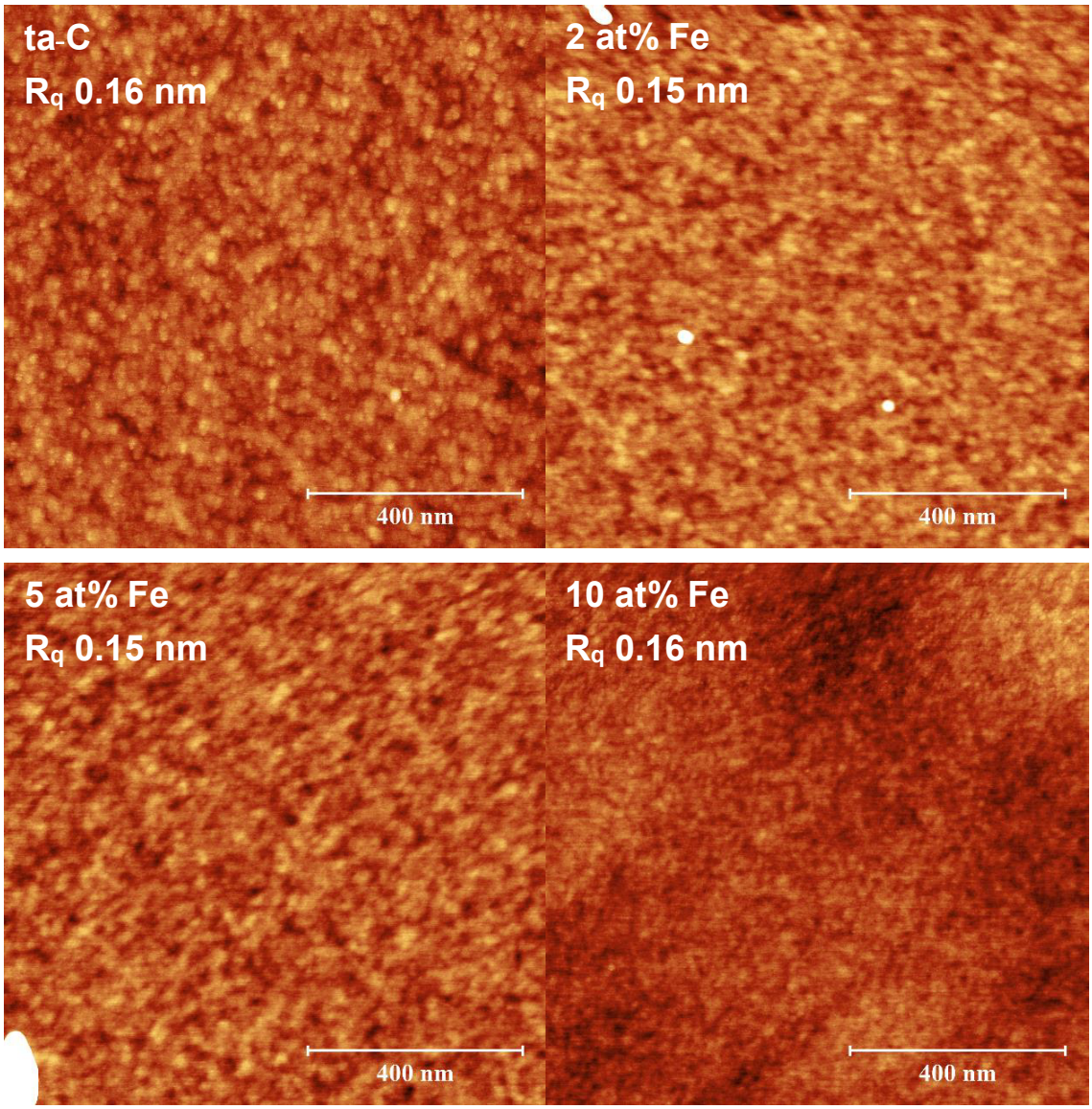

Figure 7. Atomic force microscopy height topography results of investigated samples. False color scale in all images is 2 nm. However, most of the particles seen in white are considerably larger than the scale and are therefore out of range.

Table 2. Measured root mean squared roughness values obtained by XRR and AFM.

Method	ta-C	2 at% Fe	5 at% Fe	10 at% Fe
XRR R_q (nm)	0.95	0.51	0.59	0.91
AFM R_q (nm)	0.16	0.15	0.15	0.16

As for XRR roughness in Table 2, illustrated previously in Figure 4, the film roughness appears to increase from 2 at% Fe with added iron; this is seen in the faster decrease in measured intensity with larger scan angles and increased iron content. This trend is in conflict with the reference ta-C of comparably higher roughness. Furthermore, due to the limited amount of XRR measurement resources and simulation error probability, these trends are deemed to not have significance in this context. Additionally, it should be noted that the roughness analysis by XRR compared to AFM was notably different: a) the AFM roughness was measured from an area where no major particles were present whereas the X-ray beam is incident on a comparatively much larger area, and b) the X-ray interaction volume and scattering is sensitive also to the interior of the film.

5.1.3 Crystallinity

Grazing incidence X-ray diffraction (GIXRD) was initially utilized to investigate the crystallinity of the iron deposition rate calibration samples, which revealed an expected Fe {110} peak, as shown Appendix C. GIXRD was then further utilized in an attempt to shed light on the crystallinity of the Fe/ta-C thin films. The Fe/ta-C samples, however, turned out amorphous and did not show any crystallinity in GIXRD measurements.

In order to investigate the nanoscale crystallinity, transmission electron microscopy and select area electron diffraction were used. Crystallinity was only observed for the 10 at% Fe sample, at the investigated sites. Figure 8 shows a planar bright-field high resolution TEM micrograph of the 10 at% Fe film, containing areas of apparent iron nanocrystallites of around 5 nm in diameter and some graphitic planes. The darker areas have more mass-density i.e. elements of higher density than amorphous carbon. The inset features a fast Fourier transform (FFT) of the marked area in reciprocal space with d-spacings corresponding to Fe {110} and C {002} [66, 67]. It must be noted, that evolution of graphite from amorphous carbon species is commonly expected in TEM operation under intense electron beam bombardment.

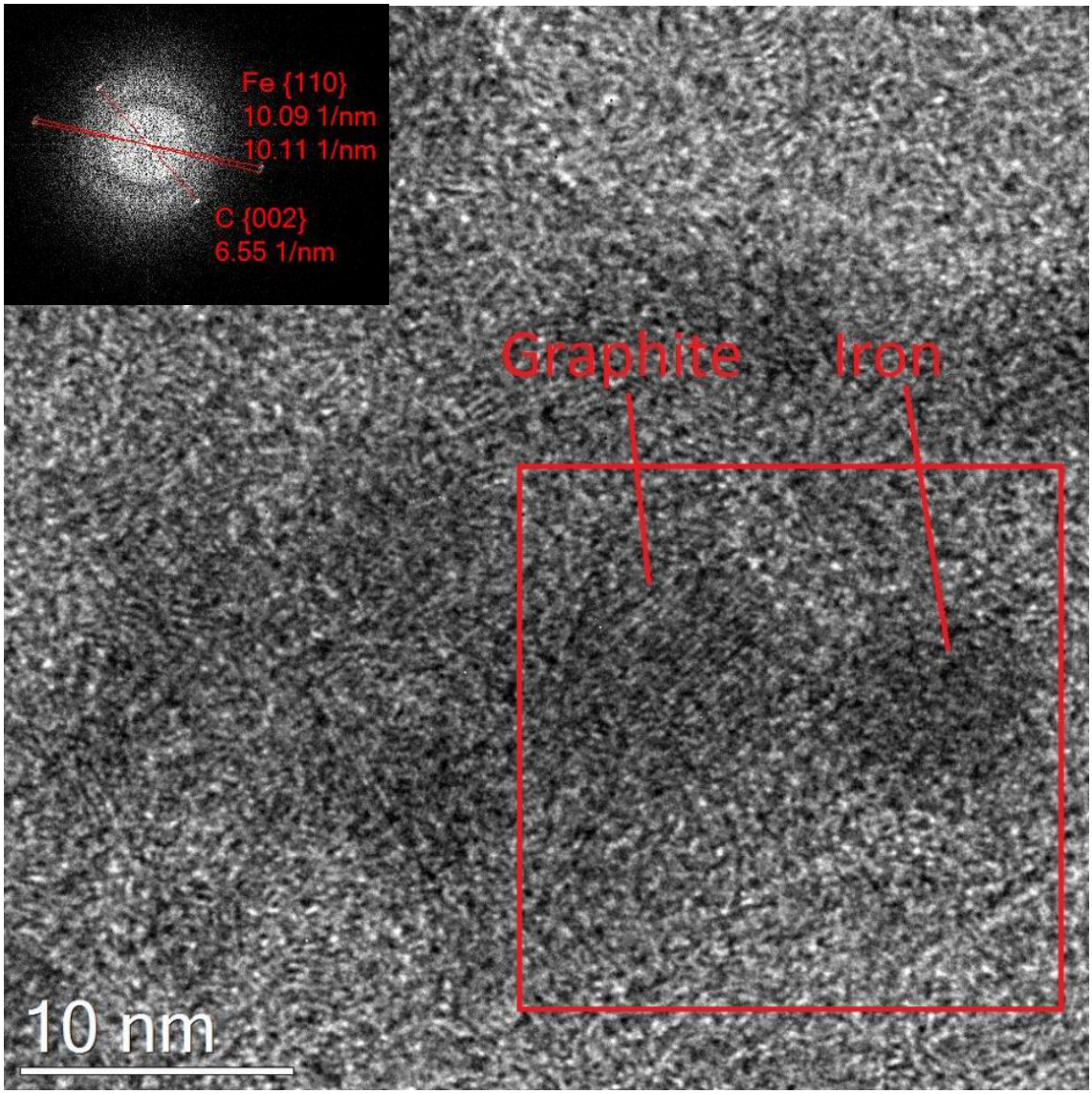

Figure 8. A planar TEM micrograph of 10 at% Fe sample showing areas of apparent iron nanocrystallites and graphitic planes. Inset shows a fast Fourier transform of the area marked in red with calculated d-spacings corresponding to Fe {110} and C {002} planes.

In addition to TEM micrographs, select area electron diffraction (SAED) patterns were obtained for areas similar to that in Figure 8. Figure 9 displays a SAED diffractogram for the 10 at% Fe sample with diffraction rings indexed for copper and iron as per literature. Table 3 also presents these diffraction patterns in comparison to reference [66, 68]. The presence of metallic copper is explained by the proximity to the underlying copper TEM grid and it does not overlap with Fe lattice planes.

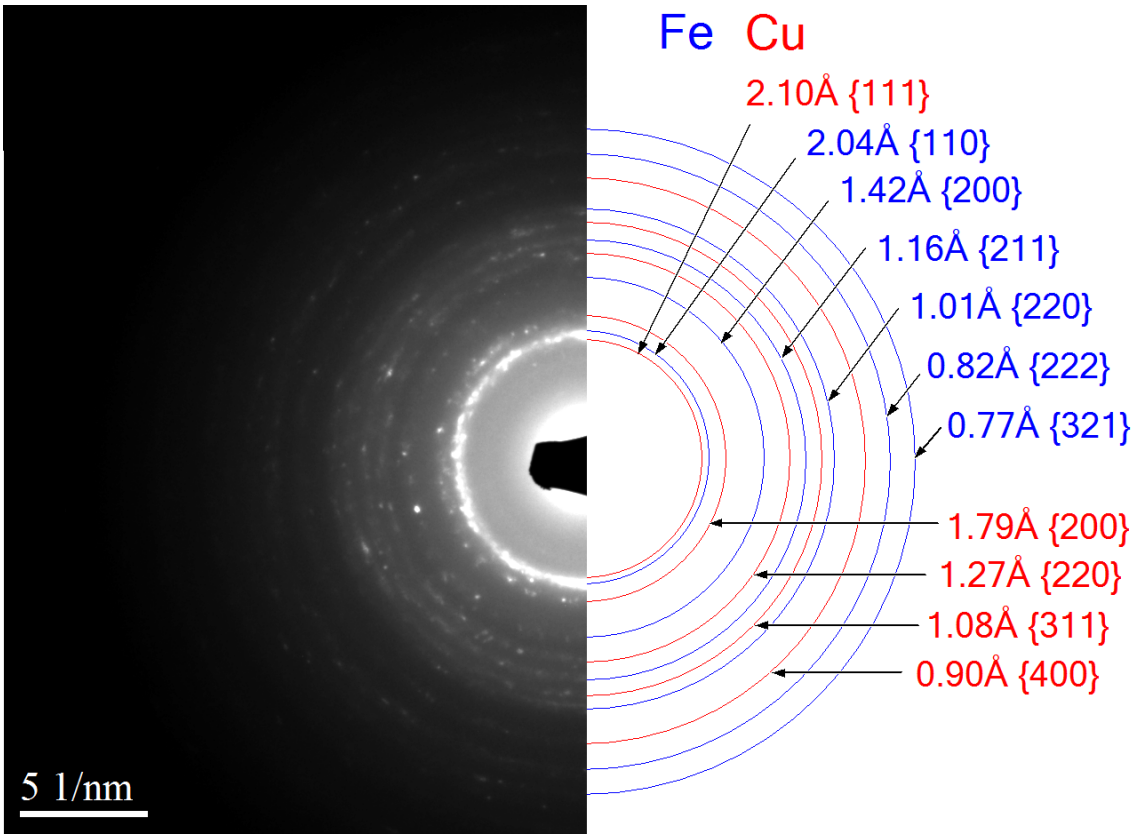

Figure 9. Select area electron diffraction pattern of the 10 at% Fe sample with corresponding d-spacings and lattice planes shown. Diffraction rings are indexed as per literature for iron and copper, also shown in Table 3. The agreement between TEM micrograph, SAED pattern, and reference values is considerably good.

SAED patterns obtained for Fe/ta-C samples of 2 and 5 at% Fe, included in Appendix D, were not found to show distinct diffraction patterns similar to Figure 9. They showed, however, a diffuse scattering pattern dissimilar to plain ta-C. Due to the local nature of TEM measurements, it is probable that 2 and 5 at% Fe samples also have crystallinity similar to 10 at% Fe.

Table 3. SAED diffraction pattern d-spacings for iron and copper with respect to reference values from literature, indexed from Figure 9.

Lattice	$d_{measured}$ (Å)	$d_{reference}$ (Å) [66, 68]
Cu {111}	2.10	2.08
Fe {110}	2.04	2.05
Cu {200}	1.79	1.80
Fe {200}	1.42	1.43
Cu {220}	1.27	1.27
Fe {211}	1.16	1.16
Cu {311}	1.08	1.08
Fe {220}	1.01	1.01
Cu {400}	0.91	0.90
Fe {222}	0.82	0.82
Fe {321}	0.77	0.76

5.1.4 Sheet Resistance

Sheet resistance measurements were conducted to determine the effect of added iron on sheet resistance. Average sheet resistances and standard deviations as error bars are plotted in Figure 10 as a function of Fe at%. These values are also tabulated in Table 4 in section 5.2.

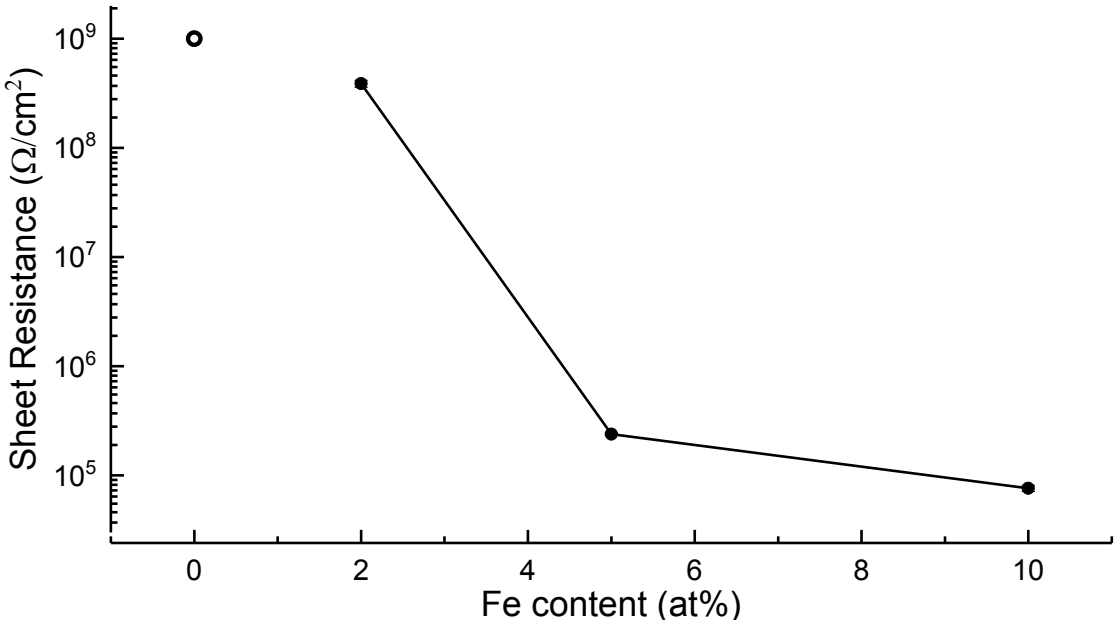

Figure 10. Four point probe average sheet resistances and standard deviations plotted as a function of Fe at%. Displayed error bars are smaller than their respective dots. Lines are drawn to guide the eye. The reference ta-C, noted with an open circle, was too resistive to be measured i.e. > 1 GΩ/cm^2.

As evident from Figure 10, the small Fe addition of 2 at% makes the film measurably more conductive compared to the insulating ta-C reference of > 1 GΩ/cm^2, which was too resistive for the Hewlett-Packard 3458A multimeter to measure. Furthermore, a successive Fe addition to 5 at% results in a resistivity reduction by three orders of magnitude. For the highest amount of 10 at% Fe, a less dramatic drop is observed.

5.1.5 Spectroscopy

Film iron content was assessed with SEM assisted by energy-dispersive X-ray spectroscopy (EDX) for supporting information. Averaged EDX iron intensities normalized to silicon intensity with standard deviations are shown in Figure 11 as a function of Fe at%. These values are also tabulated in Table 4 in section 5.2. It is evident from Figure 11 how an increase in calculated Fe at% results in a linear increase of Fe EDX signal. Reference ta-C of no added iron shows a small background noise as expected.

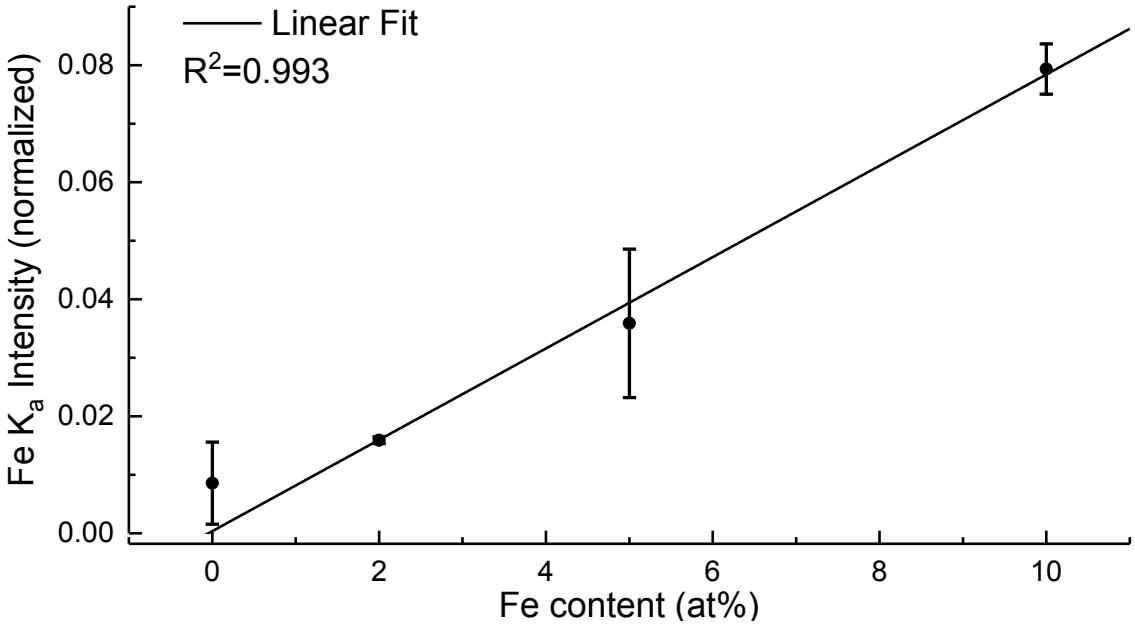

Figure 11. Averaged EDX Fe K_a peak intensities normalized to silicon as a function of Fe at%. Error bars are standard deviations calculated from the population. Linear fit shows a good correlation coefficient.

Additionally, Raman spectroscopy was used to investigate the effect of added iron on the quality of the amorphous carbon in Fe/ta-C. Raman spectra shown in Figure 12, fitted according to Ferrari et al. [55, 60, 69], show two Gaussian peaks for D and G regions of amorphous carbon. The I(D)/I(G) peak intensity ratios, representative of the sp^2 carbon bonding fractions are displayed in Figure 13 and also tabulated in Table 4 in section 5.2. The low I(D)/I(G) for the reference ta-C is representative of a typical ta-C film [61].

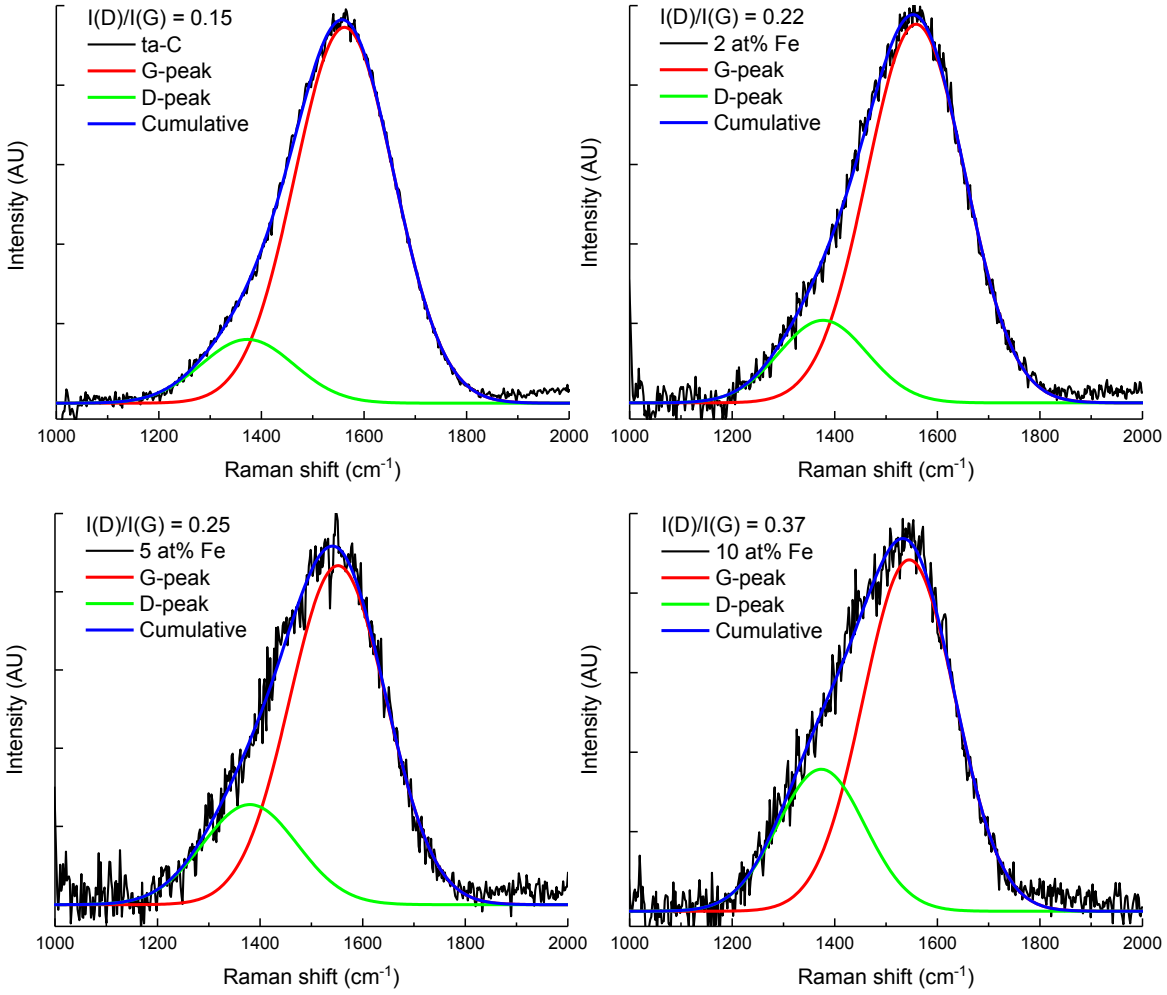

Figure 12. Obtained Raman spectra for all samples, fitted according to Ferrari et al. [60] show two Gaussian peaks for D and G regions of amorphous carbon. The I(D)/I(G) peak area intensity ratios, representative of the sp^2 carbon bonding fractions

As iron is added into the ta-C matrix, the I(D)/I(G) ratio increases indicating an increase in sp^2-clustering. Also, as shown in Figure 14, an increased amount of iron shifts the G-peak to lower wavenumbers, which is indicative of an increase in carbon bond disorder [60]. Although not shown here, the added iron attenuated the total measured signal as expected [70]. It should be noted, however, that some metals such as silver [71]

can also enhance the total received Stokes scattering signal by surface-enhanced Raman spectroscopy (SERS). For this reason it is difficult to separate the effects of SERS and attenuation caused by iron nanoparticles.

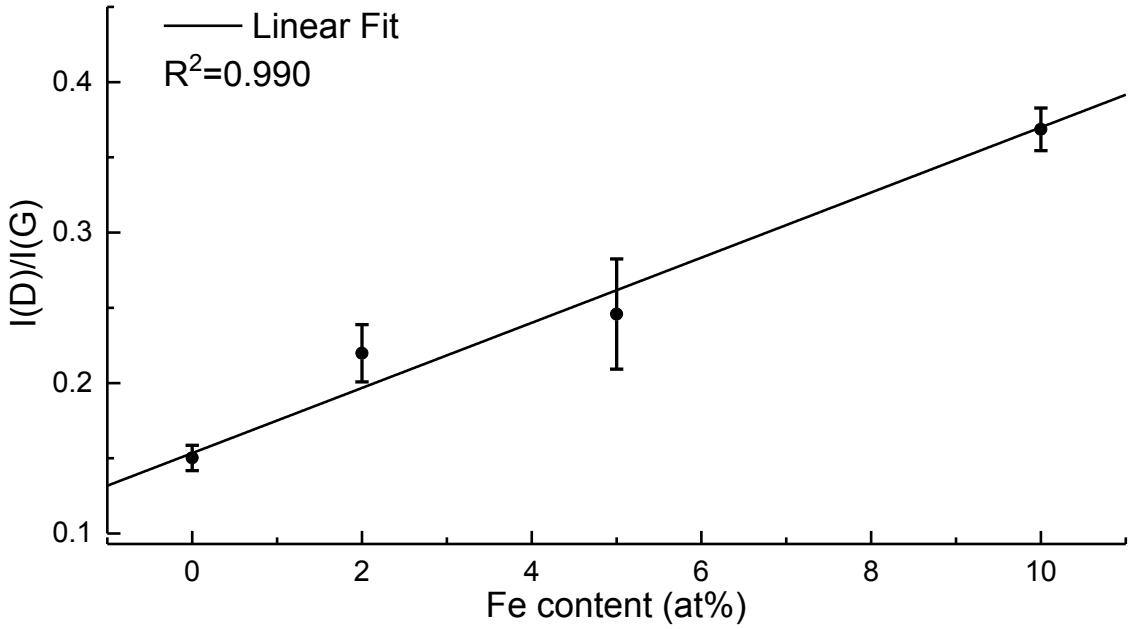

Figure 13. Averages and standard deviations of I(D)/I(G) values for Fe/ta-C samples as a function of Fe at%. A lower value signifies a higher amount of carbon sp^3-bonding. [60]

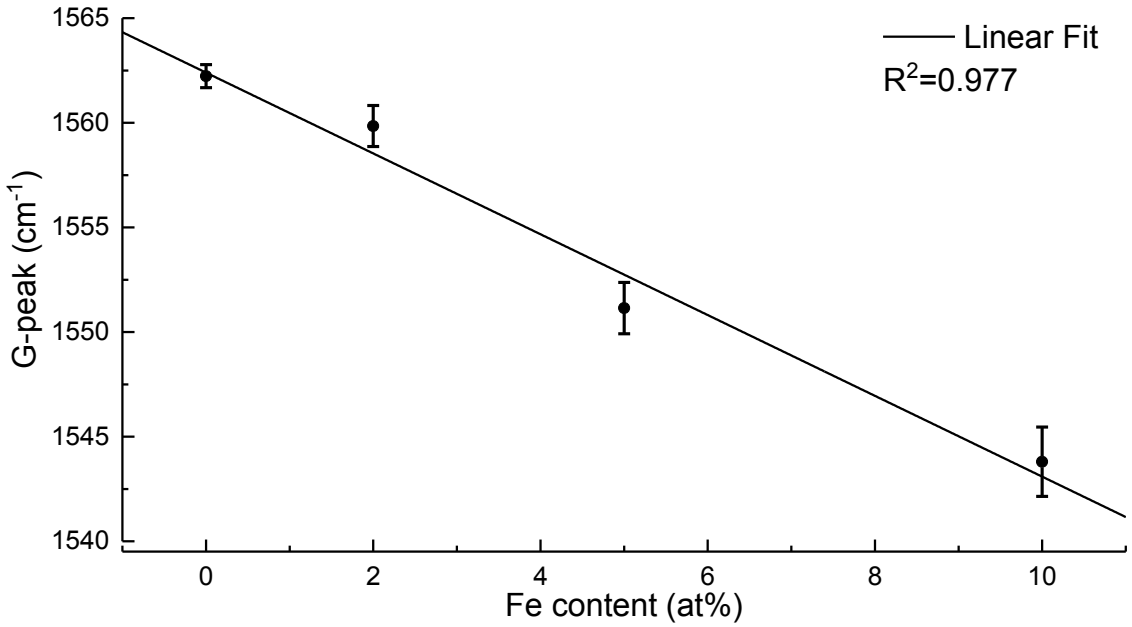

Figure 14. Averages and standard deviations of G-peak positions for Fe/ta-C samples as a function of Fe at%.

5.1.6 Film Characterization Summary Table

This subsection summarizes the results of non-electrochemical characterization methods in Table 4. The aim of Table 4 is to help the reader in comparing the results of section 5.1, to the electrochemical results presented in the following section 5.2.

Table 4. Summary of measured film characteristics for ta-C and Fe/ta-C. Additionally, the effect of added iron on the respective parameter is denoted as an increasing or decreasing arrow, when relevant.

Method	ta-C	2 at%	5 at%	10 at%	Effect of Fe
Expected Thickness (nm)	30	30	30	30	
XRR Thickness (nm)	31	29	26	29	
Profilometry Thickness (nm)	27 (5)	27 (5)	27 (2)	28 (4)	
FESEM Thickness (nm)	33 (1)	26 (1)	25 (2)	26 (1)	
XRR R_q (nm)	0.95	0.51	0.59	0.91	→
AFM R_q (nm)	0.16	0.15	0.15	0.16	→
XRR Density (g/cm^3)	2.94	3.21	3.41	3.55	↗
SEM EDX Fe-content (AU)	0.009 (0.007)	0.016 (0.001)	0.036 (0.013)	0.079 (0.004)	↗
4-point probe (Ω/cm^2)	$>1\cdot10^9$	$3.9\cdot10^8$ ($3\cdot10^7$)	$2.4\cdot10^5$ ($4\cdot10^3$)	$7.6\cdot10^4$ ($5\cdot10^3$)	↘
Raman I(D)/I(G)	0.15 (0.02)	0.22 (0.04)	0.25 (0.02)	0.37 (0.08)	↗
Raman G-peak (cm^{-1})	1562 (1)	1560 (1)	1551 (1)	1544 (2)	↘
TEM SAED Fe detection	-	indicative	indicative	yes	
HRTEM FFT Fe detection	-	-	-	yes	

5.2 Electrochemical Characteristics

This subsection first presents electrochemical characterization results from cyclic voltammetry of sulfuric acid, ascorbic acid, paracetamol, and hexaammineruthenium. Then, electrochemical impedance spectroscopy results are exhibited.

5.2.1 Sulfuric Acid

Cyclic voltammetry scans conducted in 0.15 M H_2SO_4 for 400 mV/s are displayed in Figure 15. The calculated electrochemical potential window range in water, also known as water window, is tabulated for all measured samples in Table 5.

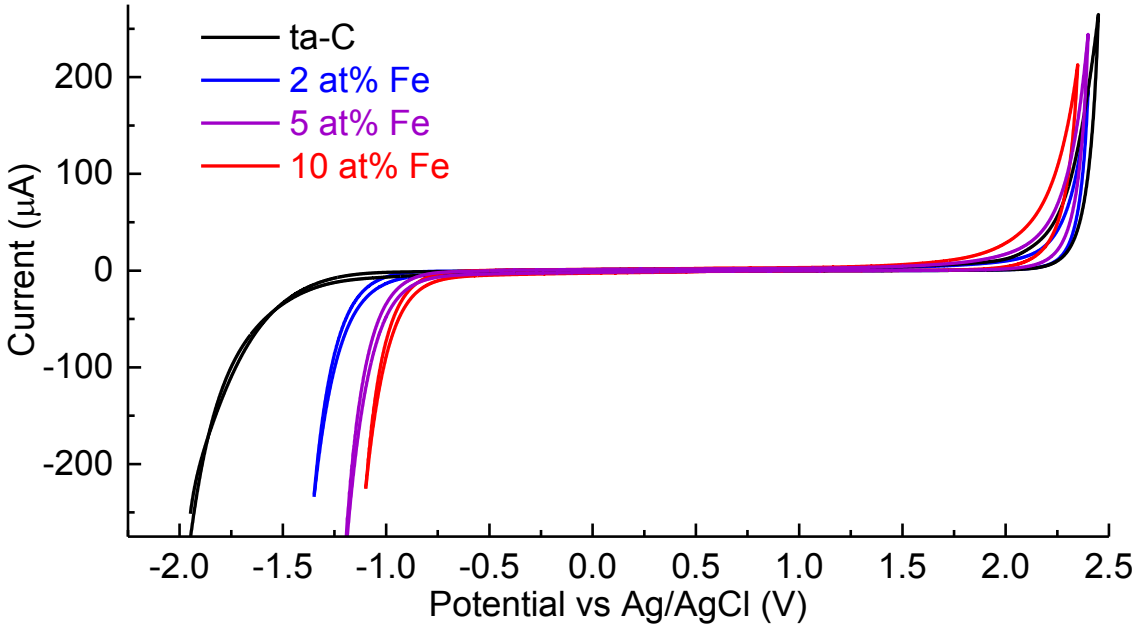

Figure 15. Cyclic voltammetry potential window results in 0.15 M H_2SO_4 for 400 mV/s at 200 μA threshold.

While there is only a minor decrease in the oxygen evolution potential as a function of Fe at%, even the slightest increase of Fe to 2 at% results in a substantial anodic shift in the hydrogen evolution potential, as noted in Table 5. From the aspect of electrochemical stability, all samples exhibit observably flat double-layer regions. Pseudo-capacitance values calculated from the potential range -200 to +200 mV are also displayed in Table 5. Subsequent additions of Fe were found to incrementally increase the pseudo-capacitance values calculated for Fe/ta-C.

Table 5. Cyclic voltammetry water window results of 0.15 M H_2SO_4 for 400 mV/s, calculated from Figure 15 for a 200 μA threshold. Anodic and cathodic potentials bounds E_{pa} and E_{pc} (V), and water window (V) are listed. Pseudo-capacitance values (μF/cm^2) were calculated as averages of 50 and 400 mV/s scan rates.

Fe at%	E_{pa}	E_{pc}	Water Window	Pseudo-capacitance
ta-C	2.42	-1.90	4.32	13.82
2	2.40	-1.33	3.73	14.24
5	2.38	-1.16	3.54	19.29
10	2.34	-1.09	3.43	21.80

5.2.2 Ascorbic Acid

Cyclic voltammetry scans of 100 and 400 mV/s conducted in 1 mM ascorbic acid are displayed in Figure 16. Oxidation peak potential values, and peak current densities (J_{pa}) for 400 and 100 mV/s scan rates are tabulated in Table 6. The ascorbic acid oxidation reaction is irreversible.

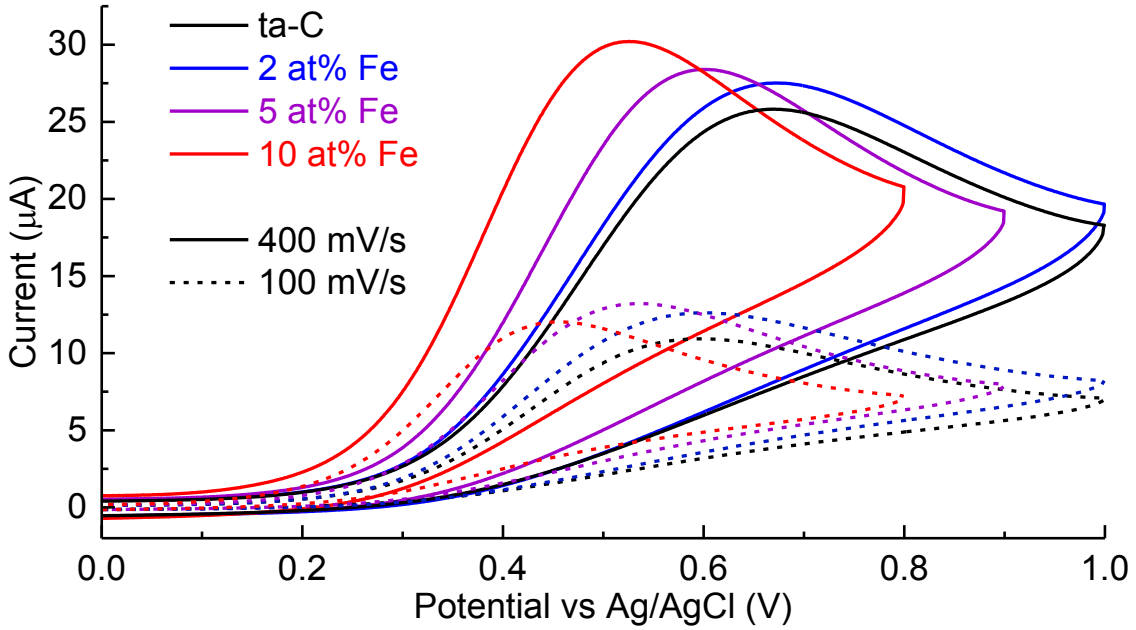

Figure 16. Cyclic voltammogram for irreversible oxidation of 1 mM ascorbic acid in PBS. Scan rates of 100 and 400 mV/s are denoted by dashed and solid lines, respectively.

Successive additions of iron are observed to induce both a cathodic oxidation potential shift, and an incremental peak current increase. Compared to reference ta-C there is a substantial increase in overall ascorbic acid electrochemical activity. Linear correlation of

peak current ($I_{p\ ox}$) as a function of $\upsilon^{(1/2)}$ indicates the oxidation reaction for all samples is diffusion limited, as displayed in Appendix E.

Table 6. Cyclic voltammetry peak potentials E_p (mV) and current densities J_p ($\mu A/cm^2$) of 1 mM ascorbic acid oxidation obtained from Figure 16 for 100 and 400 mV/s scan rates.

Fe at%	100 mV/s		400 mV/s	
	$E_{p\ ox}$	$J_{p\ ox}$	$E_{p\ ox}$	$J_{p\ ox}$
ta-C	597	145	669	360
2	599	176	672	383
5	537	182	601	392
10	457	164	526	417

5.2.3 Paracetamol

Cyclic voltammetry scans of 100 and 400 mV/s conducted in 1 mM paracetamol, also known as acetaminophen, are displayed in Figure 17. Oxidation and reduction peak potential values (E_p), and current densities (J_p) are tabulated in Table 7 for 100 and 400 mV/s. Table 8 includes peak potential separation (ΔE_p), and peak current ratios ($I_{p\ ox}/I_{p\ red}$) calculated from values in Table 7.

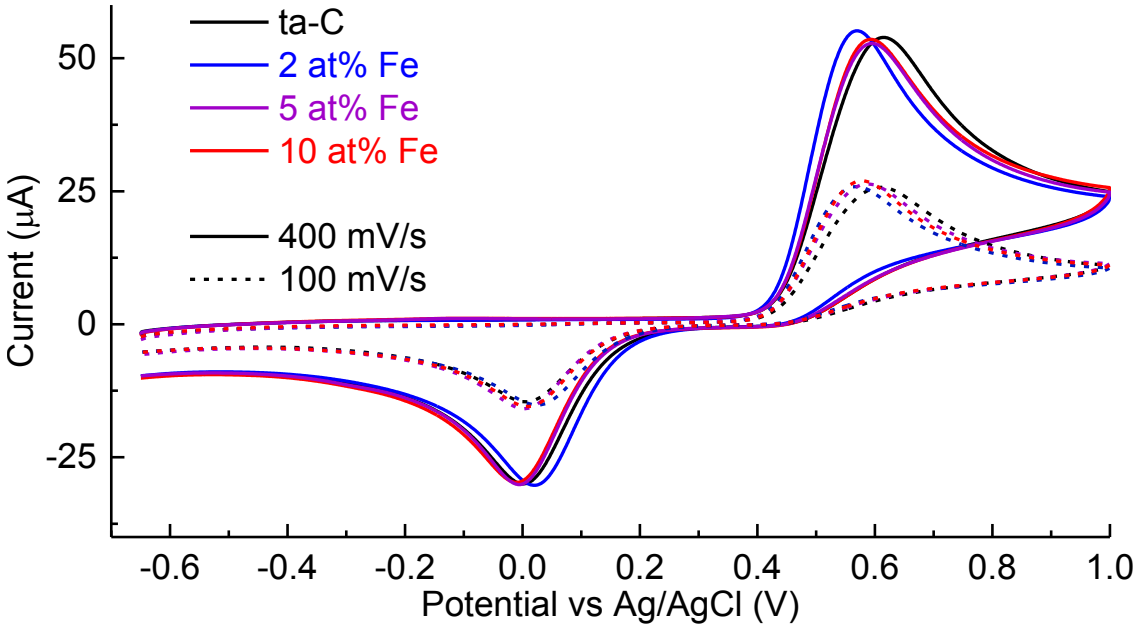

Figure 17. Cyclic voltammogram of 1 mM paracetamol in PBS. Scan rates of 100 and 400 mV/s are denoted by dashed and solid lines, respectively.

Table 7. Cyclic voltammetry peak potentials E_p (mV) and current densities J_p ($\mu A/cm^2$) for oxidation and reduction of 1 mM paracetamol. Values were calculated from Figure 17 for 100 and 400 mV/s scan rates.

Fe at%	Oxidation				Reduction			
	100 mV/s		400 mV/s		100 mV/s		400 mV/s	
	$E_{p\ ox}$	$J_{p\ ox}$	$E_{p\ ox}$	$J_{p\ ox}$	$E_{p\ red}$	$J_{p\ red}$	$E_{p\ red}$	$J_{p\ red}$
ta-C	609	355	614	739	6	187	1	399
2	567	360	569	761	23	200	20	404
5	586	358	596	722	3	213	-7	406
10	576	375	594	735	9	207	-10	400

Table 8. Cyclic voltammetry results of 1 mM paracetamol for scanning speeds of 100 and 400 mV/s, as calculated from values in Table 7: oxidation and reduction peak potential separations ΔE_p (mV), and respective peak current ratios $I_{p\ ox}/I_{p\ red}$.

Fe at%	100 mV/s		400 mV/s	
	ΔE_p	$I_{p\ ox}/I_{p\ red}$	ΔE_p	$I_{p\ ox}/I_{p\ red}$
ta-C	603	1.78	613	1.83
2	543	1.81	548	1.88
5	582	1.68	602	1.78
10	566	1.81	603	1.84

Values in Tables 7 and 8 indicate no significant differences in paracetamol electrochemical activity as a function of added iron in Fe/ta-C films. As per $I_{p\ ox}/I_{p\ red}$, the oxidation and reduction reactions are found to be quasi-reversible. This is typical for paracetamol, which usually has quasi-reversible voltammograms e.g. on boron-doped diamond electrodes [72]. Faster scanning rates or addition of iron did not have any noticeable effects on reversibility. Linear correlation of peak currents (I_p) as a function of $\upsilon^{(1/2)}$ indicate the oxidation and reduction reactions for all samples are diffusion limited, as displayed in Appendix E.

5.2.4 Hexaammineruthenium

Cyclic voltammetry scans conducted in 1 mM $Ru(NH_3)_6$ in 1 M KCl are displayed in Figure 18 with values in Table 9. Peak potentials, peak potential separation (ΔE_p), and peak current ratios ($I_{p\,ox}/I_{p\,red}$) for 400 and 100 mV/s scan rates are tabulated in Table 10.

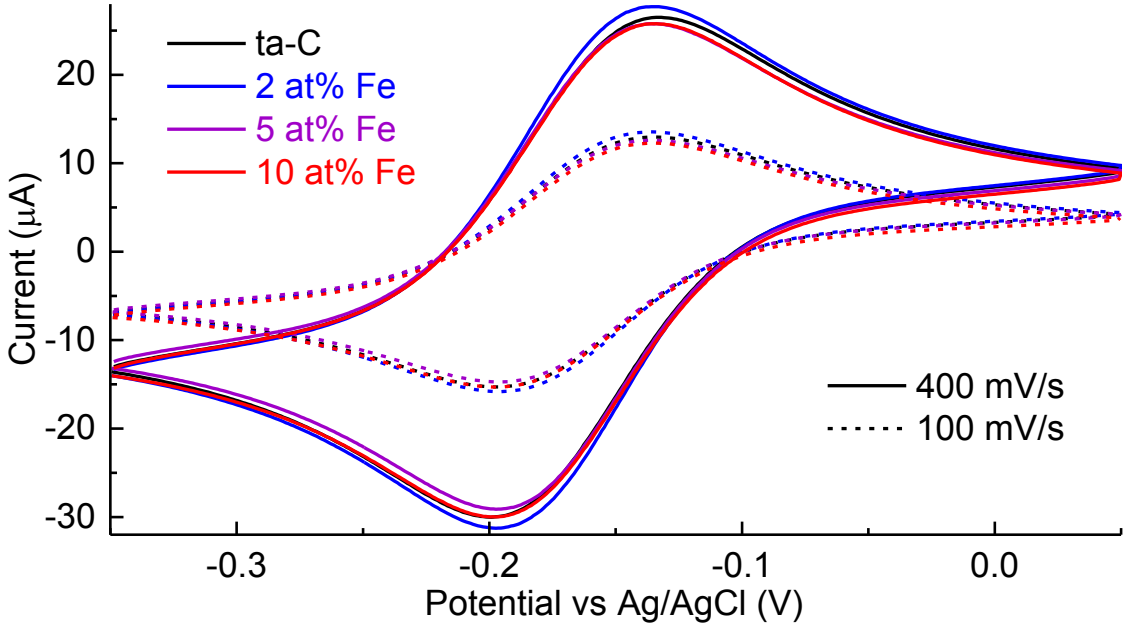

Figure 18. Cyclic voltammogram of 1 mM $Ru(NH_3)_6^{2+/3+}$ in 1 M KCl. Scan rates of 100 and 400 mV/s are denoted by dashed and solid lines, respectively.

Table 9. Cyclic voltammetry peak potentials E_p (mV) and currents J_p ($\mu A/cm^2$) for oxidation and reduction of 1 mM $Ru(NH_3)_6^{2+/3+}$. Values were calculated from Figure 18 for 100 and 400 mV/s scan rates.

Fe at%	Oxidation				Reduction			
	100 mV/s		400 mV/s		100 mV/s		400 mV/s	
	$E_{p\,ox}$	$J_{p\,ox}$	$E_{p\,ox}$	$J_{p\,ox}$	$E_{p\,red}$	$J_{p\,red}$	$E_{p\,red}$	$J_{p\,red}$
ta-C	-135	206	-132	400	-198	223	-199	444
2	-136	215	-134	420	-196	232	-197	463
5	-137	200	-134	391	-197	215	-197	430
10	-136	199	-134	390	-197	218	-200	436

Table 10. Cyclic voltammetry results of 1 mM $Ru(NH_3)_6$ for scanning speeds of 100 and 400 mV/s, as calculated from values in Table 9: oxidation and reduction peak potential separations ΔE_p (mV), and respective peak current ratios $I_{p\,ox}/I_{p\,red}$.

Fe at%	100 mV/s		400 mV/s	
	ΔE_p	$I_{p\,ox}/I_{p\,red}$	ΔE_p	$I_{p\,ox}/I_{p\,red}$
ta-C	63	0.93	68	0.90
2	63	0.93	68	0.91
5	60	0.93	64	0.91
10	61	0.91	66	0.90

It is evident from Figure 18 and Table 10 how both ΔE_p and $I_{p\,ox}/I_{p\,red}$ remain equally unchanged with added iron at both scanning speeds. This indicates that all Fe/ta-C films and the reference ta-C are close to reversible at both 100 and 400 mV/s scan rates. Also the ΔE_p values for all samples are close to ideal, albeit the small increase of 5 mV at higher scan rates, which is partially a result of uncompensated resistance in the system.

As $Ru(NH_3)_6$ is an outer-sphere redox system and as such insensitive to surface chemistry [64], there appears to be no differences in electron transfer kinetics as a function of Fe at%. Linear correlation of peak currents (I_p) as a function of $\upsilon^{(1/2)}$ indicate the oxidation and reduction reactions are diffusion limited for all samples, as displayed in Appendix E.

5.2.5 Electrochemical Impedance Spectroscopy

EIS spectra measured in 5 mM $Ru(NH_3)_6$ in 1 M KCl fitted with the modified Randles equivalent circuit is presented in Figure 19. Parameters obtained from the equivalent circuit fitting are displayed in Table 11. The higher solution resistance (R_s) values for ta-C and 10 at% Fe/ta-C are a result of the higher initial R_u value i.e. a result of electrode preparation. This can be also seen in the Figure 19 inset where the two spectrums of the two samples are located at higher Z_{real} values. The highest uncompensated resistances (R_u) measured in this study cause an iR drop of less than 3 mV. Therefore, no iR compensations were required. R_{ct} is the resistance of electron transfer to the electrode surface and through the film.

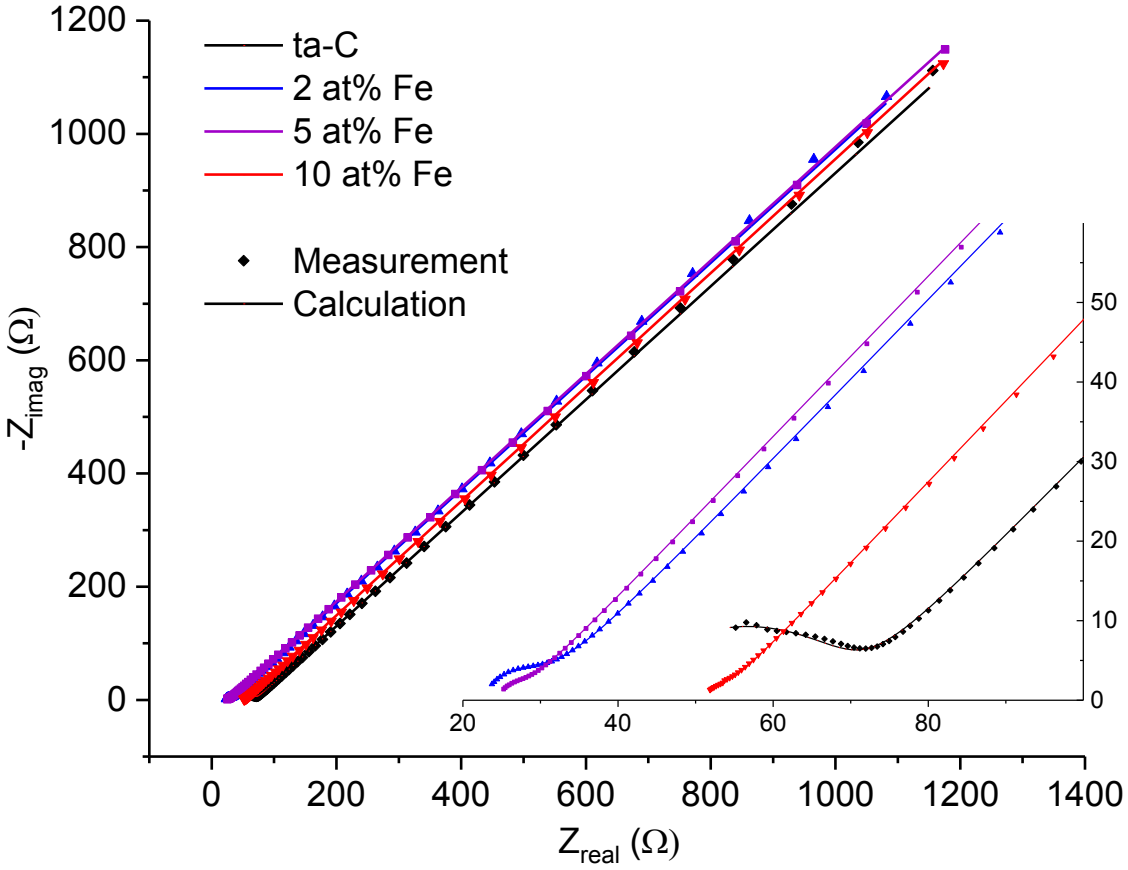

Figure 19. Nyquist plots of EIS measurements in 5 mM $Ru(NH_3)_6$ in 1 M KCl showing both experimental data (markers) and the fitted simulation (solid line). Inset shows a magnification of the high-frequency range to show the low R_{ct} values of investigated electrodes. The Z_{real} offsets are different R_u values due to electrode preparation.

Table 11. EIS results calculated from fitting the Nyquist plots in Figure 19 with the modified Randles circuit.

Fe at%	a	R_s (Ω)	R_{ct} (Ω)	C_{dl} (μF/cm^2)	k^0_{app} (cm/s)	R_u (Ω)
ta-C	0.69	40.7	29.8	0.44	0.05	54
2	0.79	22.5	8.9	5.36	0.17	22
5	0.80	24.2	4.4	5.79	0.34	25
10	0.75	50.7	4.0	6.63	0.37	40

As shown by the measured R_{ct} values in Table 11, addition of iron appears to incrementally decrease the electron transfer resistance. This correlation can be similarly applied to a substantial increase in the apparent rate constant (k^0_{app}). In contrast to the slight increase in pseudo-capacitance as calculated from sulfuric acid CV (Table 5), the double-layer capacitance (C_{dl}) values from EIS measurements show a significant increase as a function of added iron. The most noticeable increase is found for the 2 at% Fe sample exhibiting a 10-fold increase in C_{dl}. This change in C_{dl} does not appear to have an effect on a of the Randles circuit constant phase element.

6 Discussion

First, the physical properties of the films are discussed based on the obtained results. Then, the electrochemical performance is discussed with respect to the investigated analytes.

6.1 Film Characteristics

Film thickness for all samples was measured to be around the expected 30 nm, using XRR, FESEM, and profilometry. Of the three methods, XRR was deemed to be the most precise. Still, XRR can be potentially inaccurate without sufficient knowledge about the studied film structure. Therefore, profilometry and FESEM were used to verify the thickness measured by XRR.

From the characterization summary in Table 4, the XRR, FESEM, and profilometry thickness measured for each sample correspond well to each other within experimental error. However, the measured thickness for Fe/ta-C films appears slightly smaller than the reference ta-C or the expected thickness. Additionally, the measured XRR density for Fe/ta-C appears higher than expected, see Appendix A. Altogether, this may suggest that there are less carbon atoms in the film than expected. Furthermore, the Fe/ta-C film formation may be different from that of a single element film i.e. the sticking coefficient of carbon atoms to Fe/ta-C is less than that for ta-C. Nevertheless, a more likely explanation for this variance comes from uncontrollable changes in deposition rate due to variance in cathode material maintenance procedure.

Considering the actual iron content in deposited films, as plotted in Figure 11 SEM EDX is in relative agreement with expected increases in Fe at%. This trend of increased Fe at% is also reflected by an increase in XRR critical angle i.e. increased density (Figure 4), which is consistent with literature [43]. The XRR density of 2.94 g/cm^3, obtained for the reference ta-C corresponds to an sp^3 fraction of about 80%, as per Robertson [30, 55], which is a typical value for the p-FCVA process. These observations of iron content are well correlated in 4-point probe measurements, where even the smallest addition of 2 at% Fe makes the films measurably more conductive. A further iron addition to 5 at% decreases sheet resistance by three orders of magnitude. Very similar trends have been observed e.g. for Zn, Mo and W/DLC composite films [36, 45, 46].

For sheet resistance analysis, it is imperative to also account for changes in sp^2 carbon-to-carbon bonding within the ta-C structure, as this is a common mechanism of conduction in ta-C films [34]. Raman spectroscopy results in Table 4 indicate an increase

in sp^2-clustering with increased Fe-content. This change, induced by the addition of atomic or clustered iron species, may also have an effect on measured sheet resistance and electrochemical electron transfer kinetics. Additionally, based on the sp^3-formation mechanism detailed by Robertson [30], one could expect higher sp^2-content in the immediate proximity of iron nanoparticles. However, it is important to note that the Raman analysis models described by Ferrari et al. [60] are only developed for all-carbon DLC films.

The I(D)/I(G) of 0.37 (0.08) measured for the 10 at% Fe sample, is over twice that of the reference ta-C in this study, but is still well within the ranges of I(D)/I(G) values reported for ultra-thin ta-C films [32, 61, 73]. The 2 at% Fe sample has a I(D)/I(G) of 0.22 (0.04), which is comparable to that of typical ta-C [61]. This suggests low amounts of iron have minor effects on carbon bonding in ta-C. The respectively increased amount of iron in 5 and 10 at% Fe show a clear increase in I(D)/I(G) and a decrease in Raman signal intensity. The higher I(D)/I(G) with increased Fe content points to an increased amount of sp^2-clustering or total sp^2-fraction in the Fe/ta-C matrix [60]. It should be noted, that an increase in I(D)/I(G) is an indirect method of indicating an increase in total sp^2-content or in sp^2-clustering [60]. The spectral shapes of D and G-peaks in Figure 12 indicate there are no dramatic shifts from ta-C to amorphous carbon with increased Fe at% [60, 62]. Therefore, it is not strictly reliable to estimate the contribution of carbon sp^2-bonding to sheet resistance based solely on increases of I(D)/I(G).

Although the metal addition induced I(D)/I(G) increase in this study was found to be moderate, such increases can be much larger for metal-DLC composites. A study by Pasaja et al. [46] found that even the smallest addition of molybdenum (1:20 pulse ratio) increased the I(D)/I(G) to about 0.97 compared to their reference ta-C value of 0.15. Since the p-FCVA dual-cathode (Mo/ta-C) system used by Pasaja et al. was very similar to the one used in the current study, the reference I(D)/I(G) values are found identical. Moreover, the investigated pulse ratios (Mo:C) were equal: 1:10, 1:5 and 1:2, which suggests that the addition of iron does not disturb the ta-C matrix as significantly as molybdenum [46]. Yet, direct comparison can be misleading as there can be differences in deposition rates and film growth depending on the target material.

One important aspect in the electrical properties of ta-C is the existence of sp^2-rich surface layer deposited by ion implantation. Several computational [32, 34, 74], as well as XAS, XPS, and EELS studies [75, 76] have investigated the nature of ta-C and its sp^2-rich surface structures. For example, Caro et al. [74] found computationally the surface a-C to consist of clustered olefinic chains, with a lower ratio of ringed carbon structures. In

addition, XRR measurements conducted for the ta-C deposition rate calibration series, in Appendix A, support the existence of an a-C surface layer on ta-C, as also measured extensively in other studies [55, 75]. This mesoscopic surface conductivity is not in conflict with the macroscopic 4-point probe measurement results, which likely penetrate through the surface of the film being measured. In general, sheet resistance measurements of 2 at% Fe found a substantial increase in conductivity, while the I(D)/I(G) remained mostly unchanged. This implies that the increase in conductivity was most likely caused by the added iron content, for example through hopping conductivity. This is further supported by a) the 7-fold decrease in R_{ct} electron transfer resistance, and by b) the notion that I(D)/I(G) stayed within typical ta-C values [61] even for the 5 and 10 at% Fe samples (0.25 and 0.37).

As evident from FESEM images in Figure 6, the surfaces of all samples appear visually very smooth. This is also apparent from the subnanometer R_q roughness values measured by AFM. The films deposited by p-FCVA are characteristically known to be ultrasmooth with R_q values as low as 0.1 nm [32, 77, 78]. However, the roughness measured in this study by AFM is most likely limited by the fairly large tip radius of 8 nm. Unlike the common AFM tips used in this study, an expensive and fragile high resolution tip is required to measure the smallest pores between hills separated by few nanometers. Therefore, the AFM R_q roughness measured in this study underestimates the actual topography to an unknown extent. As for comparative relevance, however, the roughness is likely underestimated equally in all samples, enabling a reliable comparison between the samples. Addition of iron into ta-C film by p-FCVA showed no clear evidence of cluster formation in AFM images. Metal cluster formation is typical in DLC composites deposited by magnetron sputtering of copper, silver or gold [44, 79-81]. These differences can be due to differences in deposition rates and methods. Additionally, iron is less noble and has a tendency to form compounds with oxygen and carbon. However, no evidence of iron-carbon compounds were discovered with the characterization methods used in this study.

The AFM results are also in line with observations made in XRR measurements. Compared to AFM, however, XRR also yields information from inside the simulated layers. According to Table 4 the addition of iron increases the roughness as observed by the X-rays. This is seen in Figure 4 as a decrease in reflectivity signal as a function of measured 2-theta angle. Similar to small angle X-ray scattering (SAXS), the layer roughness causes diffuse non-specular scattering, which reduces the specular reflectivity measured [8-10, 40]. Although this may point to an increase in the number or size of iron

nanoparticles in the film, a more reliable analysis requires for example high-resolution TEM cross-section analysis. Also, the high roughness of reference ta-C compared to Fe/ta-C samples puts the validity of XRR roughness analysis and comparison into question.

High-resolution TEM micrographs in Figure 8 and SAED diffraction pattern in Figure 9 together clearly indicate the presence of Fe nanoparticles in 10 at% Fe/ta-C films. However, for the 2 and 5 at% Fe samples, no such crystallinity was observed in the measured areas, as displayed in Appendix D. Although not definitive, it is likely that there exists varying degrees of iron species crystallinity in samples of 2 and 5 at% Fe. Considering the high amounts of iron used in this study, one would expect more obvious evidence of Fe crystallinity. However, the apparent mixing of iron and carbon due to the sub-plantation phenomena [30], typical to pulsed p-FCVA processes, could partially explain the lack of readily detectable crystallinity for Fe/ta-C films. Additionally, it was unexpected to find no clear evidence of iron oxides, as iron surfaces are easily oxidized in ambient. Since the last deposition steps for Fe/ta-C were 2, 4, or 10 pulses of carbon (as per pulse ratio), it can be assumed that the embedded iron nanostructures may be protected by some layers of carbon against oxidation, similar to e.g. Tavakkoli et al. [21].

To summarize, XRR density in Table 4, and macroscopic EDX spectroscopy in Figure 11 indicate the increase of iron in Fe/ta-C films. The existence of iron nanoparticles is observed locally for 10 at% Fe in TEM micrographs in Figure 8. These results support the hypothesis of mixing, or atomic scale iron clusters embedded in ta-C films. Even the smallest addition of Fe is seen to a) dramatically increase conductivity, and b) shift ascorbic acid oxidation potential. Therefore, the presence of well dispersed and encapsulated iron in the Fe/ta-C film can be seen to explain the change in both electrical and electrochemical behavior as observed by CV and EIS.

6.2 Electrochemistry

The water window for reference ta-C, shown in Figure 15, is slightly larger than those found in literature [32]. This difference, however, is most probably due the smaller cut-off threshold and the larger electrode area i.e. lower current density used by Protopopova et al. [32]. The addition of iron had a relatively small effect on the measured water window. The anodic branch exhibits only a minor negative shift of 80 mV in total, while in the cathodic branch even the smallest increase of Fe (2 at%) results in a major positive shift of 570 mV, illustrated in Figure 15. In total, the cathodic branch shifts 810 mV, which is most likely due to the enhanced hydrogen evolution reaction kinetics, also observed by other groups for iron nanoparticles [21, 22]. All samples were electrochemically stable as indicated by their considerably flat double-layer regions in Figure 15, as compared to Protopopova et al. [32]. This stability may be due to the absence of titanium adhesion underlayer, as used by Protopopova et al, or point to evidence of iron nanostructures covered by carbon layers, as described by Tavakkoli et al. [21].

The pseudo-capacitance values measured in this study for ta-C, shown in Table 5, were substantially smaller than those observed in literature [32]. These larger values in literature [32] are potentially due to the titanium underlayer and the larger potential window used by Protopopova et al. for the pseudo-capacitance calculation. Subsequent additions of Fe were found to incrementally increase the pseudo-capacitance values for Fe/ta-C films. The contrast of high pseudo-capacitance values compared to EIS double-layer capacitance (C_{dl}) in Table 11 is likely due to the higher faradaic contribution typical to CV scans, whereas EIS measurements are conducted at formal potential with small AC signals. Nonetheless, EIS measurements indicate over an order of magnitude increase in double-layer capacitance even with the smallest addition of iron (2 at% Fe). This behavior may be similar to SWCNT supercapacitors [82], which have 27 at% Fe embedded. Even if SWCNT iron content would have an effect on capacitance, such direct comparison to Fe/ta-C can be pointedly unpredictable due to enormous differences in surface areas.

Ascorbic acid (AA) and its oxidation by iron ions and complexes is highly dependent on pH [11]. In this study both AA and paracetamol (PA) were studied in pH 7.4 PBS, where AA exists mostly in its ascorbate anion form [11]. This is why some electrode modifications aim to block the negatively charged AA anions and attract positively charged analytes by tailoring the electrode surface charge to be more negative [16]. Although catalytic mechanisms of iron complexes with AA are exhaustively discussed by e.g. Valko et al. [83, 84], detailed examination of mechanisms for electrochemical activity

of iron towards AA is beyond the scope of this work due to limited electrochemical and surface chemistry characterization.

In this work, the ascorbic acid oxidation potential on ta-C was measured to be about 600 mV for 100 mV/s, as tabulated in Table 6. Compared to previous studies by Sainio et al. [76], this is a relatively high oxidation potential for ta-C but can be explained by the larger film thickness used in this study. As detailed by Palomäki et al. [61], increased thickness of ta-C induces slower electron transfer kinetics. Successive additions of iron were observed to induce both a negative AA oxidation potential shift from 600 mV to about 450 mV, and a 12 % increase in peak current (100 mV/s). This decrease in AA oxidation overpotential and increase in oxidation current suggests enhanced electron transfer kinetics with added iron. In literature [6], iron oxide-graphene modification of glassy carbon was found to similarly shift the AA oxidation peak away from the overlapping dopamine peak.

Sainio et al. [76] have shown that distribution of surface oxygen containing functional groups may shift the oxidation potential and electrochemical activity of AA and dopamine measured on 7 nm thick ta-C electrodes. However, they also found the 15 nm ta-C to have slower outer sphere redox reactions. When applied to Fe/ta-C, this reasoning may suggest changes in the surface distribution of oxygen containing functional groups. However, making a direct comparison is unfeasible, since the electrodes in the current study are 30 nm thick, and the thickness of ta-C film affects electron transfer kinetics [32]. Further investigations by X-ray photoelectron spectroscopy (XPS) or X-ray absorption spectroscopy (XAS) are required to determine the oxygen content and loading of iron species on the surface of Fe/ta-C film.

In the current study, no differences were found in $Ru(NH_3)_6$ outer sphere redox reaction with added iron content, as all the electrodes were already reversible (Table 10). Additionally, the 30 nm thick reference ta-C film was also found to be reversible, which is not typical. For example in a study by Protopopova et al. [32] 30 nm thick ta-C films were found non-reversible in ferrocenemethanol. The effect of added iron was revealed in more sensitive EIS measurements shown in Table 11 as an enhancement in electron transfer resistance (R_{ct}), apparent rate constant (k^0_{app}), and double-layer capacitance (C_{dl}). Typically, such enhancements can be attributed to increased surface area. However, as evident from AFM results (Table 4), the surface roughness i.e. surface area remained constant with addition of iron. This may imply, that the enhancement in electron transfer kinetics observed in water window and AA oxidation can be either due

to AA-specific electrochemical behavior of surface iron, or due to general enhancement of electron transfer kinetics throughout the Fe/ta-C films.

The paracetamol (PA) oxidation potential for reference ta-C was measured to be around 600 mV in this study, as tabulated in Table 7. This value is found to be similar to glassy carbon [85], but slightly less than that for e.g. boron-doped diamond (BDD) [72]. Excluding glassy carbon, sp^2-materials with defective graphene sheets, such as CNTs and graphene oxide, have a lower oxidation potential for PA [8, 9, 72, 86]. As proposed by Kang et al. the PA redox reaction can be catalyzed by materials facilitating favorable π-π interactions [86]. In this study, the addition of iron into ta-C films was not found to shift the PA oxidation potential. It is therefore implied, that no formation of graphene defect-like π-orbital structures were induced on Fe/ta-C film surface. Similar behavior of PA with respect to iron can be observed in literature by comparing studies where iron was added into a graphene nanostructure (oxidation potential around 300 mV) [7], to studies where PA was detected by plain graphene nanostructures, also at around 300 mV [86]. A direct comparison, however, is somewhat unfeasible as the studies were conducted at slightly different pH levels, which similar to AA affects the oxidation potential of PA [9, 86].

An important result of this study, the ineffectiveness of iron in shifting PA oxidation away from the relatively high potential of 600 mV is both desirable and relevant. Firstly, addition of iron to ta-C films gradually shifts the oxidation potential of AA from 600 mV to 450 mV i.e. away from the PA oxidation potential. This occurs while the anodic end of the water window remains substantially wide at +2.34 V. Secondly, the oxidation potential of another common interferant, uric acid (UA), is commonly in the range of 200 to 400 mV for carbon nanostructure electrodes [5, 17], and iron containing carbon nanostructures [7, 87]. Therefore, by adding iron into ta-C electrodes, the oxidation peaks of inner sphere analytes AA, UA, and PA appear to separate. Additionally, this result underlines the point, that the surface of the Fe/ta-C films is not modified since all these reaction are surface chemistry driven. The sensitivity and selectivity of these inner sphere analytes can be routinely increased by utilizing differential pulse voltammetry (DPV).

7 Conclusions

Iron was added into ta-C thin films for tailoring of electrical and electrochemical properties by fabricating Fe/ta-C thin films with three different Fe at%, namely 2, 5, and 10 at%. These films were co-deposited using room temperature p-FCVA process to deposit ta-C thin films tailored with embedded iron nanoparticles. Unlike relevant studies, addition of iron did not result in deposition of sp^2-rich a-C. Increased iron content induced the formation of TEM observable non-oxidized iron nanocrystallites in 10 at% Fe/ta-C. Hence, the iron nanoparticles are assumed to be protected from ambient oxidation by deposited top-layers of carbon. To the best knowledge of the author, herein described Fe/ta-C thin films are as of yet unreported.

With incremental additions of iron, the anodic end of the water window remained unchanged, while the cathodic end exhibited an anodic shift. For AA oxidation potential, a cathodic shift and an increase in peak current was recorded. This shift enhanced the selectivity between AA and PA, since the oxidation potential of PA remained unaffected. Thus, addition of iron into ta-C thin films increased both the sensitivity and selectivity of the investigated API detection measurement. To further improve this selectivity compared to used voltammetric techniques, DPV measurements are in progress. For future *in vitro* applications of Fe/ta-C thin films in API detection, DPV is among the most sensitive and selective electrochemical techniques for direct evaluation of analyte concentrations.

Compared to ta-C thin films, Fe/ta-C films had increased double-layer capacitance, enhanced electron transfer kinetics, dramatically lowered sheet resistance, and comparable electrochemical stability. Related to literature, these improvements in electrical and electrochemical properties are similar to those observed for crystalline iron or iron oxide nanoparticles in carbon nanostructures. In order to further control iron nanoparticle formation in Fe/ta-C films, *in situ* heat treatments during p-FCVA deposition and GIXRD measurement will be performed. Such heat treatments are expected to influence both sp^2-bonding and iron crystallinity. These implications can be further used to tailor application driven physicochemical properties of Fe/ta-C in *in vivo* and *in vitro* sensors. In order to shed light on the effect of iron on ta-C carbon bonding, composition, and structure, spectroscopic techniques such as EELS or XAS analysis should be performed.

Since many relevant analytes and interferants are dependent on surface inner sphere electron transfer, XPS investigations are underway to determine the iron loading and

oxygen content on the electrode surface. Further analysis of iron content throughout the film should be carried out by XRF or SIMS to accurately quantify the film composition.

The investigated Fe/ta-C thin films offer considerable added benefit compared to ta-C films for *in vitro* electrochemical detection of APIs and neurotransmitters. It is also inferred from the results, that iron or iron oxides in carbon nanostructures have a distinct electrochemical behavior. It is imperative to take this effect into account for example in sensor applications where trace amounts of iron exist from the initial fabrication process.

References

[1] H. A. Gasteiger, S. S. Kocha, B. Sompalli, and F. T. Wagner, "Activity benchmarks and requirements for Pt, Pt-alloy, and non-Pt oxygen reduction catalysts for PEMFCs", *Appl. Catal. B Environ.*, vol. 56, no. 1-2, pp. 9-35, Mar. 2005, doi:10.1016/j.apcatb.2004.06.021.

[2] M. Tavakkoli, T. Kallio, O. Reynaud, A. G. Nasibulin, J. Sainio, H. Jiang, E. I. Kauppinen, and K. Laasonen, "Maghemite nanoparticles decorated on carbon nanotubes as efficient electrocatalysts for the oxygen evolution reaction", *J. Mater. Chem. A*, vol. 4, no. 14, pp. 5216-5222, 2016, doi:10.1039/C6TA01472K.

[3] A. Moisala, A. G. Nasibulin, and E. I. Kauppinen, "The role of metal nanoparticles in the catalytic production of single-walled carbon nanotubes-a review", *J. Phys. Condens. Matter*, vol. 15, no. 42, pp. S3011-S3035, Oct. 2003, doi:10.1088/0953-8984/15/42/003.

[4] A. G. Nasibulin, P. V. Pikhitsa, H. Jiang, D. P. Brown, A. V. Krasheninnikov, *et al.*, "A novel hybrid carbon material", *Nat. Nanotechnol.*, vol. 2, no. 3, pp. 156-161, Mar. 2007, doi:10.1038/nnano.2007.37.

[5] P. Kanchana, S. Radhakrishnan, M. Navaneethan, M. Arivanandhan, Y. Hayakawa, and C. Sekar, "Electrochemical Sensor Based on Fe Doped Hydroxyapatite-Carbon Nanotubes Composite for L-Dopa Detection in the Presence of Uric Acid", *J. Nanosci. Nanotechnol.*, vol. 16, no. 6, pp. 6185-6192, Jun. 2016, doi:10.1166/jnn.2016.11645.

[6] T. Peik-See, A. Pandikumar, H. Nay-Ming, L. Hong-Ngee, and Y. Sulaiman, "Simultaneous electrochemical detection of dopamine and ascorbic acid using an iron oxide/reduced graphene oxide modified glassy carbon electrode", *Sensors (Basel).*, vol. 14, no. 8, pp. 15227-15243, 2014, doi:10.3390/s140815227.

[7] M. Liu, Q. Chen, C. Lai, Y. Zhang, J. Deng, H. Li, and S. Yao, "A double signal amplification platform for ultrasensitive and simultaneous detection of ascorbic acid, dopamine, uric acid and acetaminophen based on a nanocomposite of ferrocene thiolate stabilized Fe3O4@Au nanoparticles with graphene sheet", *Biosens. Bioelectron.*, vol. 48, pp. 75-81, Oct. 2013, doi:10.1016/j.bios.2013.03.070.

[8] S. Cheemalapati, S. Palanisamy, V. Mani, and S. M. Chen, "Simultaneous

electrochemical determination of dopamine and paracetamol on multiwalled carbon nanotubes/graphene oxide nanocomposite-modified glassy carbon electrode", *Talanta*, vol. 117, pp. 297-304, 2013, doi:10.1016/j.talanta.2013.08.041.

[9] R. N. Goyal, V. K. Gupta, and S. Chatterjee, "Voltammetric biosensors for the determination of paracetamol at carbon nanotube modified pyrolytic graphite electrode", *Sensors Actuators B Chem.*, vol. 149, no. 1, pp. 252-258, Aug. 2010, doi:10.1016/j.snb.2010.05.019.

[10] S. Sainio, T. Palomäki, S. Rhode, M. Kauppila, O. Pitkänen, *et al.*, "Carbon nanotube (CNT) forest grown on diamond-like carbon (DLC) thin films significantly improves electrochemical sensitivity and selectivity towards dopamine", *Sensors Actuators, B Chem.*, vol. 211, pp. 177-186, 2015, doi:10.1016/j.snb.2015.01.059.

[11] K. A. Skov and D. J. Vonderschmitt, "Kinetics of iron and copper catalysis of ascorbate oxidation.", *Bioinorg. Chem.*, vol. 4, no. 3, pp. 199-213, Apr. 1975.

[12] A. Rosanoff, G. M. Briggs, and B. O. De Lumen, "Corrosion of iron by ascorbic acid and catalysis of ascorbate oxidation by products of the iron corrosion", *J. Agric. Food Chem.*, vol. 33, no. 5, pp. 891-896, Sep. 1985, doi:10.1021/jf00065a031.

[13] J. Aronovitch, D. Godinger, A. Samuni, and G. Czapski, "Ascorbic Acid Oxidation and DNA Scission Catalyzed by Iron and Copper Chelates", *Free Radic. Res. Commun.*, vol. 2, no. 4-6, pp. 241-258, Jan. 1987, doi:10.3109/10715768709065289.

[14] E. Peltola, N. Wester, K. B. Holt, L.-S. Johansson, J. Koskinen, V. Myllymäki, and T. Laurila, "Nanodiamonds on tetrahedral amorphous carbon significantly enhance dopamine detection and cell viability", *Biosens. Bioelectron.*, vol. 88, pp. 273-282, Feb. 2017, doi:10.1016/j.bios.2016.08.055.

[15] E. Kaivosoja, E. Berg, A. Rautiainen, T. Palomaki, J. Koskinen, M. Paulasto-Krockel, and T. Laurila, "Improving the function of dopamine electrodes with novel carbon materials", *Conf. Proc. Annu. Int. Conf. IEEE Eng. Med. Biol. Soc. IEEE Eng. Med. Biol. Soc. Annu. Conf.*, vol. 2013, pp. 632-634, Jul. 2013, doi:10.1109/EMBC.2013.6609579.

[16] E. Rand, A. Periyakaruppan, Z. Tanaka, D. A. Zhang, M. P. Marsh, *et al.*, "A carbon nanofiber based biosensor for simultaneous detection of dopamine and

serotonin in the presence of ascorbicacid", *Biosens. Bioelectron.*, vol. 42, pp. 434-438, 2013, doi:10.1016/j.bios.2012.10.080.

[17] J. Ping, J. Wu, Y. Wang, and Y. Ying, "Simultaneous determination of ascorbic acid, dopamine and uric acid using high-performance screen-printed graphene electrode", *Biosens. Bioelectron.*, vol. 34, no. 1, pp. 70-76, 2012, doi:10.1016/j.bios.2012.01.016.

[18] B. I. Kharisov, O. V Kharissova, H. V. Rasika Dias, U. Ortiz Mendez, I. G. de la Fuente, Y. Pena, and A. Vazquez Dimas, "Iron-based Nanomaterials in the Catalysis", in *Advanced Catalytic Materials - Photocatalysis and Other Current Trends*, InTech, 2016, pp. 37-68.

[19] J. A. Varnell, E. C. M. Tse, C. E. Schulz, T. T. Fister, R. T. Haasch, J. Timoshenko, A. I. Frenkel, and A. A. Gewirth, "Identification of carbon-encapsulated iron nanoparticles as active species in non-precious metal oxygen reduction catalysts", *Nat. Commun.*, vol. 7, p. 12582, Aug. 2016, doi:10.1038/ncomms12582.

[20] S. Ratso, I. Kruusenberg, A. Sarapuu, P. Rauwel, R. Saar, *et al.*, "Enhanced oxygen reduction reaction activity of iron-containing nitrogen-doped carbon nanotubes for alkaline direct methanol fuel cell application", *J. Power Sources*, vol. 332, pp. 129-138, Nov. 2016, doi:10.1016/j.jpowsour.2016.09.069.

[21] M. Tavakkoli, T. Kallio, O. Reynaud, A. G. Nasibulin, C. Johans, J. Sainio, H. Jiang, E. I. Kauppinen, and K. Laasonen, "Single-Shell Carbon-Encapsulated Iron Nanoparticles: Synthesis and High Electrocatalytic Activity for Hydrogen Evolution Reaction", *Angew. Chemie Int. Ed.*, vol. 54, no. 15, pp. 4535-4538, Apr. 2015, doi:10.1002/anie.201411450.

[22] M. Tavakkoli, T. Kallio, O. Reynaud, A. G. Nasibulin, J. Sainio, H. Jiang, E. I. Kauppinen, and K. Laasonen, "Maghemite nanoparticles decorated on carbon nanotubes as efficient electrocatalysts for the oxygen evolution reaction", *J. Mater. Chem. A*, vol. 4, no. 14, pp. 5216-5222, 2016, doi:10.1039/C6TA01472K.

[23] M. Li, X. Bo, Y. Zhang, C. Han, and L. Guo, "Comparative study on the oxygen reduction reaction electrocatalytic activities of iron phthalocyanines supported on reduced graphene oxide, mesoporous carbon vesicle, and ordered mesoporous

carbon", *J. Power Sources*, vol. 264, pp. 114-122, Oct. 2014, doi:10.1016/j.jpowsour.2014.04.101.

[24] N. Atar, T. Eren, M. L. Yola, H. Karimi-Maleh, and B. Demirdogen, "Magnetic iron oxide and iron oxide@gold nanoparticle anchored nitrogen and sulfur-functionalized reduced graphene oxide electrocatalyst for methanol oxidation", *RSC Adv.*, vol. 5, no. 33, pp. 26402-26409, 2015, doi:10.1039/C5RA03735B.

[25] H. R. Byon, J. Suntivich, and Y. Shao-Horn, "Graphene-Based Non-Noble-Metal Catalysts for Oxygen Reduction Reaction in Acid", *Chem. Mater.*, vol. 23, no. 15, pp. 3421-3428, Aug. 2011, doi:10.1021/cm2000649.

[26] K. Jurkschat, X. Ji, A. Crossley, R. G. Compton, and C. E. Banks, "Super-washing does not leave single walled carbon nanotubes iron-free.", *Analyst*, vol. 132, no. 1, pp. 21-23, 2007, doi:10.1039/b615824b.

[27] T. Laurila, S. Sainio, H. Jiang, N. Isoaho, J. E. Koehne, J. Etula, J. Koskinen, and M. Meyyappan, "Application-Specific Catalyst Layers: Pt-Containing Carbon Nanofibers for Hydrogen Peroxide Detection", *ACS Omega*, vol. 2, no. 2, pp. 496-507, Feb. 2017, doi:10.1021/acsomega.6b00441.

[28] N. Tujunen, E. Kaivosoja, V. Protopopova, J. J. Valle-Delgado, M. Osterberg, J. Koskinen, and T. Laurila, "Electrochemical detection of hydrogen peroxide on platinum-containing tetrahedral amorphous carbon sensors and evaluation of their biofouling properties", *Mater. Sci. Eng. C*, vol. 55, pp. 70-78, Oct. 2015, doi:10.1016/j.msec.2015.05.060.

[29] S. Sainio, T. Palomäki, N. Tujunen, V. Protopopova, J. Koehne, K. Kordas, J. Koskinen, M. Meyyappan, and T. Laurila, "Integrated Carbon Nanostructures for Detection of Neurotransmitters", *Mol. Neurobiol.*, vol. 52, no. 2, pp. 859-866, Oct. 2015, doi:10.1007/s12035-015-9233-z.

[30] J. Robertson, "Diamond-like amorphous carbon", *Mater. Sci. Eng. R Reports*, vol. 37, no. 4-6, pp. 129-281, May 2002, doi:10.1016/S0927-796X(02)00005-0.

[31] N. Wester, S. Sainio, T. Palomäki, D. Nordlund, V. K. Singh, L.-S. Johansson, J. Koskinen, and T. Laurila, "Partially Reduced Graphene Oxide Modified Tetrahedral Amorphous Carbon Thin-Film Electrodes as a Platform for Nanomolar Detection of Dopamine", *J. Phys. Chem. C*, vol. 121, no. 14, pp. 8153-

8164, Apr. 2017, doi:10.1021/acs.jpcc.6b13019.

[32] V. S. Protopopova, N. Wester, M. A. Caro, P. G. Gabdullin, T. Palomäki, T. Laurila, and J. Koskinen, "Ultrathin undoped tetrahedral amorphous carbon films: thickness dependence of the electronic structure and implications for their electrochemical behaviour", *Phys. Chem. Chem. Phys.*, vol. 17, no. 14, pp. 9020-9031, 2015, doi:10.1039/C4CP05855K.

[33] V. S. Veerasamy, G. A. J. Amaratunga, C. A. Davis, W. I. Milne, P. Hewitt, and M. Weiler, "Electronic density of states in highly tetrahedral amorphous carbon", *Solid. State. Electron.*, vol. 37, no. 2, pp. 319-326, Feb. 1994, doi:10.1016/0038-1101(94)90084-1.

[34] M. A. Caro, R. Zoubkoff, O. Lopez-Acevedo, and T. Laurila, "Atomic and electronic structure of tetrahedral amorphous carbon surfaces from density functional theory: Properties and simulation strategies", *Carbon N. Y.*, vol. 77, pp. 1168-1182, 2014, doi:10.1016/j.carbon.2014.06.060.

[35] K. Zhou, P. Ke, X. Li, Y. Zou, and A. Wang, "Microstructure and electrochemical properties of nitrogen-doped DLC films deposited by PECVD technique", *Appl. Surf. Sci.*, vol. 329, pp. 281-286, Feb. 2015, doi:10.1016/j.apsusc.2014.12.162.

[36] K. Baba, R. Hatada, and Y. Tanaka, "Preparation and properties of W-containing diamond-like carbon films by magnetron plasma source ion implantation", *Surf. Coatings Technol.*, vol. 201, no. 19-20, pp. 8362-8365, Aug. 2007, doi:10.1016/j.surfcoat.2006.02.086.

[37] A. Iyer, J. Etula, Y. Ge, X. Liu, and J. Koskinen, "Nanodiamond embedded ta-C composite film by pulsed filtered vacuum arc deposition from a single target", *Appl. Phys. Lett.*, vol. 109, no. 20, 2016, doi:10.1063/1.4967985.

[38] A. J. Bard and L. R. Faulkner, "Electrochemical methods : fundamentals and applications", *John Wiley Sons, Inc.*, p. 833, 2001.

[39] R. S. Nicholson, "Theory and Application of Cyclic Voltammetry for Measurement of Electrode Reaction Kinetics.", *Anal. Chem.*, vol. 37, no. 11, pp. 1351-1355, Oct. 1965, doi:10.1021/ac60230a016.

[40] S. Kohli, C. D. Rithner, P. K. Dorhout, A. M. Dummer, and C. S. Menoni, "Comparison of nanometer-thick films by x-ray reflectivity and spectroscopic

ellipsometry", *Rev. Sci. Instrum.*, vol. 76, no. 2, pp. 1-5, 2005, doi:10.1063/1.1848660.

[41] S. Meskinis, A. Vasiliauskas, K. Slapikas, G. Niaura, R. Juskenas, M. Andrulevicius, and S. Tamulevicius, "Structure of the silver containing diamond like carbon films: Study by multiwavelength Raman spectroscopy and XRD", *Diam. Relat. Mater.*, vol. 40, pp. 32-37, Nov. 2013, doi:10.1016/j.diamond.2013.09.004.

[42] R. Gudaitis, S. Meskinis, K. Slapikas, M. Andrulevicius, G. Niaura, and S. Tamulevicius, "Piezoresistive and electrical properties of Cr containing diamond-like carbon films", *Surf. Coatings Technol.*, vol. 211, pp. 80-83, Oct. 2012, doi:10.1016/j.surfcoat.2011.08.040.

[43] A. Jurkeviciute, A. Lazauskas, T. Tamulevicius, A. Vasiliauskas, D. Peckus, S. Meskinis, and S. Tamulevicius, "Structure and density profile of diamond-like carbon films containing copper: Study by X-ray reflectivity, transmission electron microscopy, and spectroscopic ellipsometry", *Thin Solid Films*, vol. 630, pp. 48-58, May 2017, doi:10.1016/j.tsf.2016.10.015.

[44] S. Meskinis, A. Ciegis, A. Vasiliauskas, K. Slapikas, R. Gudaitis, I. Yaremchuk, V. Fitio, Y. Bobitski, and S. Tamulevicius, "Annealing Effects on Structure and Optical Properties of Diamond-Like Carbon Films Containing Silver", *Nanoscale Res. Lett.*, vol. 11, no. 1, p. 146, Dec. 2016, doi:10.1186/s11671-016-1362-4.

[45] H. Wong, Y. M. Foong, and D. H. C. Chua, "Improving the conductivity of diamond-like carbon films with zinc doping and its material properties", *Appl. Surf. Sci.*, vol. 257, no. 22, pp. 9616-9620, Sep. 2011, doi:10.1016/j.apsusc.2011.06.082.

[46] N. Pasaja, S. Sansongsiri, S. Intarasiri, T. Vilaithong, and A. Anders, "Mo-containing tetrahedral amorphous carbon deposited by dual filtered cathodic vacuum arc with selective pulsed bias voltage", *Nucl. Instruments Methods Phys. Res. Sect. B Beam Interact. with Mater. Atoms*, vol. 259, no. 2, pp. 867-870, Jun. 2007, doi:10.1016/j.nimb.2007.02.093.

[47] J. Ilavsky and P. R. Jemian, "Irena: Tool suite for modeling and analysis of small-angle scattering", *J. Appl. Crystallogr.*, vol. 42, no. 2, pp. 347-353, 2009, doi:10.1107/S0021889809002222.

[48] M. Bjorck and G. Andersson, "GenX: An extensible X-ray reflectivity refinement program utilizing differential evolution", *J. Appl. Crystallogr.*, vol. 40, no. 6, pp. 1174-1178, 2007, doi:10.1107/S0021889807045086.

[49] X. Zhou, S. Chen, and N. E. W. York, "Theoretical Foundation of X-ray and Neutron Reflectometry", *Phys. Rep.*, vol. 257, no. 4-5, pp. 223-348, 1995, doi:http://dx.doi.org/10.1016/0370-1573(94)00110-O.

[50] E. Piscopiello, L. Tapfer, M. V. Antisari, P. Paiano, P. Prete, and N. Lovergine, "Formation of epitaxial gold nanoislands on (100) silicon", *Phys. Rev. B*, vol. 78, no. 3, p. 35305, Jul. 2008, doi:10.1103/PhysRevB.78.035305.

[51] S. J. C. Weiss, M. Rumpel, M. Schnabel, P. Loper, "Summary for Policymakers", in *Climate Change 2013 - The Physical Science Basis*, vol. 1542, no. 9, Intergovernmental Panel on Climate Change, Ed. Cambridge: Cambridge University Press, 2013, pp. 1-30.

[52] J. Eymery, F. Leroy, and F. Fournel, "GIXRD of nanoscale strain patterning in wafer bonding", *Nucl. Instruments Methods Phys. Res. Sect. B Beam Interact. with Mater. Atoms*, vol. 200, pp. 73-78, Jan. 2003, doi:10.1016/S0168-583X(02)01677-4.

[53] L. K. Bekessy, N. A. Raftery, and S. Russell, "Anomalous Scattering from Single Crystal Substrate", *Adv. X-ray Anal*, vol. 50, pp. 177-181, 2007.

[54] M. Morita, T. Ohmi, E. Hasegawa, M. Kawakami, and M. Ohwada, "Growth of native oxide on a silicon surface", *J. Appl. Phys.*, vol. 68, no. 3, pp. 1272-1281, 1990, doi:10.1063/1.347181.

[55] A. C. Ferrari, A. Libassi, B. K. Tanner, V. Stolojan, J. Yuan, L. M. Brown, S. E. Rodil, B. Kleinsorge, and J. Robertson, "Density, sp3 fraction, and cross-sectional structure of amorphous carbon films determined by x-ray reflectivity and electron energy-loss spectroscopy", *Phys. Rev. B*, vol. 62, no. 16, pp. 11089-11103, Oct. 2000, doi:10.1103/PhysRevB.62.11089.

[56] D. M. Solina, R. W. Cheary, F. A. Lupscha, and P. D. Swift, "An Investigation of Metal Thin Films Using X-ray Reflectivity and Atomic Force Microscopy", *Adv. X-ray Anal.*, vol. 40, 1997.

[57] A. Matsutani, K. Nishioka, and M. Sato, "Energy dispersive X-ray spectroscopy

analysis of Si sidewall surface etched by deep-reactive ion etching", *Jpn. J. Appl. Phys.*, vol. 55, no. 6S1, p. 06GH05, Jun. 2016, doi:10.7567/JJAP.55.06GH05.

[58] J. L. Hutter and J. Bechhoefer, "Calibration of atomic- force microscope tips", *Rev. Sci. Instrum.*, vol. 64, no. 7, pp. 1868-1873, Jul. 1993, doi:10.1063/1.1143970.

[59] J. S. Villarrubia, "Algorithms for scanned probe microscope image simulation, surface reconstruction, and tip estimation", *J. Res. Natl. Inst. Stand. Technol.*, vol. 102, no. 4, p. 425, 1997, doi:10.6028/jres.102.030.

[60] A. C. Ferrari and J. Robertson, "Interpretation of Raman spectra of disordered and amorphous carbon", *Phys. Rev. B*, vol. 61, no. 20, pp. 14095-14107, May 2000, doi:10.1103/PhysRevB.61.14095.

[61] T. Palomäki, N. Wester, M. A. Caro, S. Sainio, V. Protopopova, J. Koskinen, and T. Laurila, "Electron transport determines the electrochemical properties of tetrahedral amorphous carbon (ta-C) thin films", *Electrochim. Acta*, vol. 225, pp. 1-10, Jan. 2017, doi:10.1016/j.electacta.2016.12.099.

[62] T. Palomäki, N. Wester, L.-S. Johansson, M. Laitinen, H. Jiang, *et al.*, "Characterization and Electrochemical Properties of Oxygenated Amorphous Carbon (a-C) Films", *Electrochim. Acta*, vol. 220, pp. 137-145, Dec. 2016, doi:10.1016/j.electacta.2016.10.063.

[63] R. G. Compton, E. Laborda, and K. R. Ward, *Understanding Voltammetry*. I, 2014.

[64] R. L. McCreery, "Advanced carbon electrode materials for molecular electrochemistry", *Chem. Rev.*, vol. 108, no. 7, pp. 2646-2687, 2008, doi:10.1021/cr068076m.

[65] C. H. Hsu and F. Mansfeld, "Technical Note: Concerning the Conversion of the Constant Phase Element Parameter Y 0 into a Capacitance", *Corrosion*, vol. 57, no. 9, pp. 747-748, Sep. 2001, doi:10.5006/1.3280607.

[66] W. P. Davey, "Precision Measurements of the Lattice Constants of Twelve Common Metals", *Phys. Rev.*, vol. 25, no. 6, pp. 753-761, Jun. 1925, doi:10.1103/PhysRev.25.753.

[67] M.-C. Lin, M. Gong, B. Lu, Y. Wu, D.-Y. Wang, *et al.*, "An ultrafast rechargeable

aluminium-ion battery", *Nature*, vol. 520, no. 7547, pp. 324-328, Apr. 2015, doi:10.1038/nature14340.

[68] A. W. Hull., "A New Method of X-Ray Crystal Analysis", *Phys. Rev.*, vol. 10, no. 6, pp. 661-696, Dec. 1917, doi:10.1103/PhysRev.10.661.

[69] A. C. Ferrari and J. Robertson, "Resonant Raman spectroscopy of disordered, amorphous, and diamondlike carbon", *Phys. Rev. B*, vol. 64, no. 7, p. 75414, Jul. 2001, doi:10.1103/PhysRevB.64.075414.

[70] D. D. Allred, Q. Wang, and J. Gonzalez-Hernandez, "Characterization of Metal/Carbon Multilayers by Raman Spectroscopy", *MRS Proc.*, vol. 160, p. 605, Jan. 1989, doi:10.1557/PROC-160-605.

[71] S. Meskinis, T. Tamulevicius, G. Niaura, K. Slapikas, A. Vasiliauskas, O. Ulcinas, and S. Tamulevicius, "Surface Enhanced Raman Scattering Effect in Diamond Like Carbon Films Containing Ag Nanoparticles", *J. Nanosci. Nanotechnol.*, vol. 16, no. 9, pp. 10143-10151, Sep. 2016, doi:10.1166/jnn.2016.12848.

[72] B. C. Lourencao, R. A. Medeiros, R. C. Rocha-Filho, L. H. Mazo, and O. Fatibello-Filho, "Simultaneous voltammetric determination of paracetamol and caffeine in pharmaceutical formulations using a boron-doped diamond electrode", *Talanta*, vol. 78, no. 3, pp. 748-752, 2009, doi:10.1016/j.talanta.2008.12.040.

[73] R. McCann, S. S. Roy, P. Papakonstantinou, G. Abbas, and J. A. McLaughlin, "The effect of thickness and arc current on the structural properties of FCVA synthesised ta-C and ta-C:N films", *Diam. Relat. Mater.*, vol. 14, no. 3-7, pp. 983-988, 2005, doi:10.1016/j.diamond.2004.12.037.

[74] M. A. Caro, J. Määttä, O. Lopez-Acevedo, and T. Laurila, "Energy band alignment and electronic states of amorphous carbon surfaces in vacuo and in aqueous environment", *J. Appl. Phys.*, vol. 117, no. 3, p. 34502, Jan. 2015, doi:10.1063/1.4905915.

[75] C. A. Davis, G. A. J. Amaratunga, and K. M. Knowles, "Growth Mechanism and Cross-Sectional Structure of Tetrahedral Amorphous Carbon Thin Films", *Phys. Rev. Lett.*, vol. 80, no. 15, pp. 3280-3283, Apr. 1998, doi:10.1103/PhysRevLett.80.3280.

[76] S. Sainio, D. Nordlund, M. A. Caro, R. Gandhiraman, J. Koehne, N. Wester, J.

Koskinen, M. Meyyappan, and T. Laurila, "Correlation between sp3-to-sp2 Ratio and Surface Oxygen Functionalities in Tetrahedral Amorphous Carbon (ta-C) Thin Film Electrodes and Implications of Their Electrochemical Properties", *J. Phys. Chem. C*, vol. 120, no. 15, pp. 8298-8304, Apr. 2016, doi:10.1021/acs.jpcc.6b02342.

[77] M. Moseler, "The Ultrasmoothness of Diamond-like Carbon Surfaces", *Science (80.).*, vol. 309, no. 5740, pp. 1545-1548, Sep. 2005, doi:10.1126/science.1114577.

[78] V. Protopopova, A. Iyer, N. Wester, A. Kondrateva, S. Sainio, T. Palomäki, T. Laurila, M. Mishin, and J. Koskinen, "Ultrathin undoped tetrahedral amorphous carbon films: The role of the underlying titanium layer on the electronic structure", *Diam. Relat. Mater.*, vol. 57, pp. 43-52, Aug. 2015, doi:10.1016/j.diamond.2015.06.009.

[79] I. Yaremchuk, S. Meskinis, V. Fitio, Y. Bobitski, K. Slapikas, A. Ciegis, Z. Balevicius, A. Selskis, and S. Tamulevicius, "Spectroellipsometric characterization and modeling of plasmonic diamond-like carbon nanocomposite films with embedded Ag nanoparticles", *Nanoscale Res. Lett.*, vol. 10, no. 1, p. 157, Dec. 2015, doi:10.1186/s11671-015-0854-y.

[80] S. Meskinis, A. Ciegis, A. Vasiliauskas, A. Tamuleviciene, K. Slapikas, R. Juskenas, G. Niaura, and S. Tamulevicius, "Plasmonic properties of silver nanoparticles embedded in diamond like carbon films: Influence of structure and composition", *Appl. Surf. Sci.*, vol. 317, pp. 1041-1046, Oct. 2014, doi:10.1016/j.apsusc.2014.09.032.

[81] S. Meskinis, A. Ciegis, A. Vasiliauskas, K. Slapikas, T. Tamulevicius, A. Tamuleviciene, and S. Tamulevicius, "Optical properties of diamond like carbon films containing copper, grown by high power pulsed magnetron sputtering and direct current magnetron sputtering: Structure and composition effects", *Thin Solid Films*, vol. 581, pp. 48-53, Apr. 2015, doi:10.1016/j.tsf.2014.11.045.

[82] P. Kanninen, N. D. Luong, L. H. Sinh, I. V Anoshkin, A. Tsapenko, J. Seppälä, A. G. Nasibulin, and T. Kallio, "Transparent and flexible high-performance supercapacitors based on single-walled carbon nanotube films", *Nanotechnology*, vol. 27, no. 23, p. 235403, Jun. 2016, doi:10.1088/0957-4484/27/23/235403.

[83] M. Valko, H. Morris, and M. Cronin, "Metals, Toxicity and Oxidative Stress", *Curr. Med. Chem.*, vol. 12, no. 10, pp. 1161-1208, May 2005, doi:10.2174/0929867053764635.

[84] M. Valko, C. J. Rhodes, J. Moncol, M. Izakovic, and M. Mazur, "Free radicals, metals and antioxidants in oxidative stress-induced cancer", *Chem. Biol. Interact.*, vol. 160, no. 1, pp. 1-40, Mar. 2006, doi:10.1016/j.cbi.2005.12.009.

[85] O. W. Lau, S. F. Luk, and Y. M. Cheung, "Simultaneous Determination of Ascorbic Acid, Caffeine and Paracetamol in Drug Formulations by Differential-pulse Voltammetry Using a Glassy Carbon Electrode", *Analyst*, vol. 114, no. September, pp. 1047-1051, 1989, doi:10.1039/an9891401047.

[86] X. Kang, J. Wang, H. Wu, J. Liu, I. A. Aksay, and Y. Lin, "A graphene-based electrochemical sensor for sensitive detection of paracetamol", *Talanta*, vol. 81, no. 3, pp. 754-759, 2010, doi:10.1016/j.talanta.2010.01.009.

[87] H. Teymourian, A. Salimi, and S. Khezrian, "Fe3O4 magnetic nanoparticles/reduced graphene oxide nanosheets as a novel electrochemical and bioeletrochemical sensing platform", *Biosens. Bioelectron.*, vol. 49, pp. 1-8, Nov. 2013, doi:10.1016/j.bios.2013.04.034.

Appendix A. Calibration Series X-ray Reflectivity Results and Comparison

This appendix summarizes additional experimental XRR results on FCVA deposition rate calibration series of iron and ta-C, shown in Figure A1 and Tables A1 and A2. Figure A2 shows the calculated deposition rates in thickness, plotted as linear regressions for iron and ta-C. Molar deposition rates can be calculated using the parameters tabulated in Tables A1 and A2.

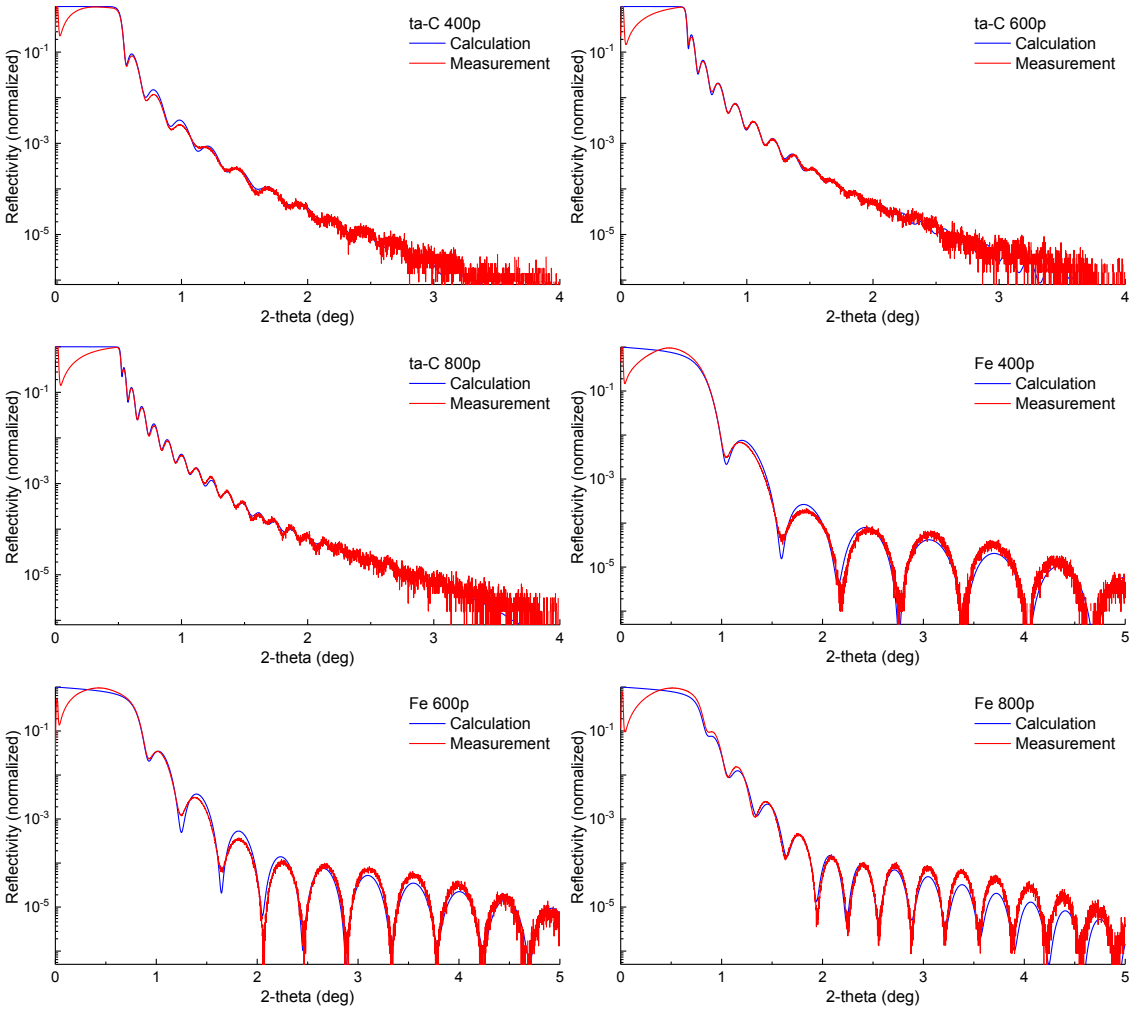

Figure A1. FCVA deposition rate calibration series. X-ray reflectivity scans of ta-C (ta-C 400p, 600p, and 800 pulses) and iron (Fe 400p, 600p, and 800 pulses) showing experimental and simulation data in red and blue, respectively. Tables A1 and A2 show the corresponding XRR layer parameters.

Table A1. X-ray reflectivity results of ta-C calibration samples (ta-C 400p, ta-C 600p, and ta-C 800p) calculated from Figure A1. Complete XRR simulation profiles are shown comprising surface a-C and core ta-C layers: thickness t (nm), density ρ (g/cm^3), roughness R_q (nm). Red values denote fixed parameters.

	ta-C 400p			ta-C 600p			ta-C 800p		
Layer	t	ρ	R_q	t	ρ	R_q	t	ρ	R_q
a-C	1.38	1.92	0.79	1.93	2.26	0.68	2.95	2.76	0.74
ta-C	34.27	2.97	2.47	50.20	3.05	1.30	63.58	3.07	0.10
SiO_2	2.00	2.20	2.01	0.39	2.20	1.43	1.64	2.20	1.81
Si	0.00	2.33	0.81	0.00	2.33	0.00	0.00	2.33	0.96

Table A2. X-ray reflectivity results of iron calibration samples (Fe 400p, Fe 600p, and Fe 800p) calculated from Figure A1. Complete XRR layer profiles are shown of 3 separately simulated iron layers of different properties: thickness t (nm), density ρ (g/cm^3), roughness R_q (nm). Red values denote fixed parameters.

	Fe 400p			Fe 600p			Fe 800p		
Layer	t	ρ	R_q	t	ρ	R_q	t	ρ	R_q
Fe 1	1.24	6.15	1.88	0.04	6.44	1.78	1.88	3.15	0.35
Fe 2	11.31	7.87	0.35	17.18	7.90	0.02	23.25	7.80	1.12
Fe 3	2.02	4.51	1.16	1.87	5.04	0.88	0.30	3.75	2.00
SiO_2	1.10	2.20	0.00	1.00	2.20	0.00	1.40	2.20	0.00
Si	0.00	2.33	0.00	0.00	2.33	0.00	0.00	2.33	0.00

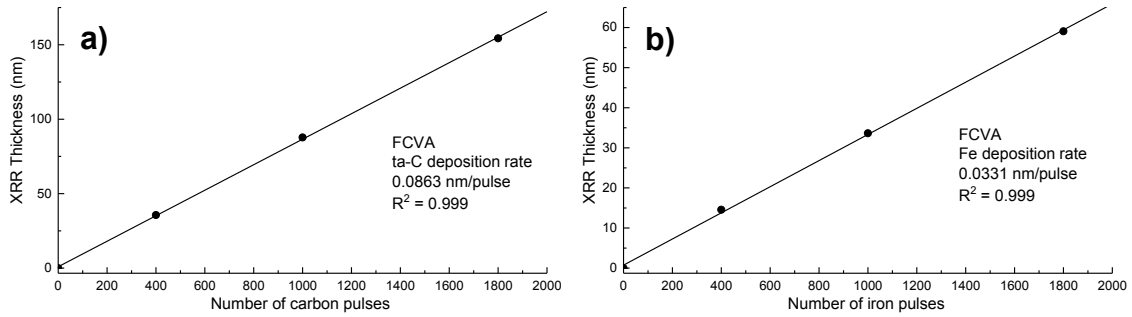

Figure A2. FCVA thickness deposition rates plotted as linear regressions for a) ta-C, and b) iron. Intersection of y-axis is equal to zero.

Table A3 summarizes Tables A1 and A2 to show the relative changes in total film thickness and average density. Since calibration series samples of ta-C include a surface a-C layer, and iron samples consist of multiple Fe layers of different densities, average densities in Table A3 were calculated as a thickness-weighted average.

Table A3. FCVA deposition rate calibration summary ta-C and Fe. Average XRR density is calculated as a thickness-weighted average.

Sample type	Total XRR Thickness (nm)	Average XRR Density (g/cm^3)	Deposition rate (nm/pulse)
ta-C 400p	35.66	2.93	
ta-C 600p	52.13	3.02	0.0863
ta-C 800p	66.53	3.05	
Fe 400p	14.56	7.26	
Fe 600p	19.08	7.62	0.0331
Fe 800p	25.43	7.41	

To evaluate the soundness of the deposition rates calculated above, the expected density and thickness values of Fe/ta-C will be compared to XRR results in Figure 4. Table A4 compares the expected vs. measured Fe/ta-C density and thickness values from X-ray reflectivity results. It should be noted, that the 2 and 5 at% Fe samples are significantly more dense than expected based on deposition rate calibration series in Tables A1, A2, and A3. The XRR critical angle measurement with the subsequent simulation can be considered a reliable way to determine thin film density.

Table A4. Comparison of expected vs. measured Fe/ta-C density and thickness values from XRR. Especially the 2 and 5 at% Fe samples are significantly more dense than expected based on deposition rate calibration series in Tables A1, A2, and A3.

	Expected		Measured	
Sample	Density (g/cm^3)	Thickness (nm)	Density (g/cm^3)	Thickness (nm)
ta-C	2.90	30	2.94	30.82
2 at% Fe	3.03	30	3.21	28.64
5 at% Fe	3.25	30	3.41	26.11
10 at% Fe	3.52	30	3.55	28.57

The full XRR layer profiles for measured Fe/ta-C samples and reference ta-C are exhibited in Tables A5 and A6, respectively. The XRR simulations were single layers of Fe/ta-C with the expected Fe at% used as the atomic composition of the layer simulation. The ta-C reference was simulated without the surface a-C layer.

Table A5. Complete XRR profiles for the primary Fe/ta-C samples, as displayed in Figure 4. Different layer profiles were developed for each Fe/ta-C layer of different Fe:C composition. Thickness t (nm), density ρ (g/cm^3), roughness R_q (nm). Red values denote fixed parameters.

Fe/taC sample	2 at% Fe			5 at% Fe			10 at% Fe		
Layer	t	ρ	R_q	t	ρ	R_q	t	ρ	R_q
2 at% Fe:C	28.64	3.21	0.51						
5 at% Fe:C				26.11	3.41	0.59			
10 at% Fe:C							28.57	3.55	0.91
SiO_2	0.56	2.20	1.36	0.28	2.20	1.51	0.44	2.20	1.26
Si	0.00	2.33	0.40	0.00	2.33	0.00	0.00	2.33	1.74

Table A6. Complete XRR profiles for the ta-C reference simulated without the surface a-C layer, as displayed in Figure 4. Thickness t (nm), density ρ (g/cm^3), roughness R_q (nm). Red values denote fixed parameters.

	Reference ta-C		
Layer	t	ρ	R_q
ta-C	30.82	2.94	0.95
SiO_2	0.56	2.20	1.21
Si	0.00	2.33	0.60

Appendix B. Additional Atomic Force Microscope Results

This appendix exhibits the additional 5x5 μm AFM scans of the Fe/ta-C and reference ta-C sample, displayed in Figure B1. Also, the presence and origin of macroparticles is debated.

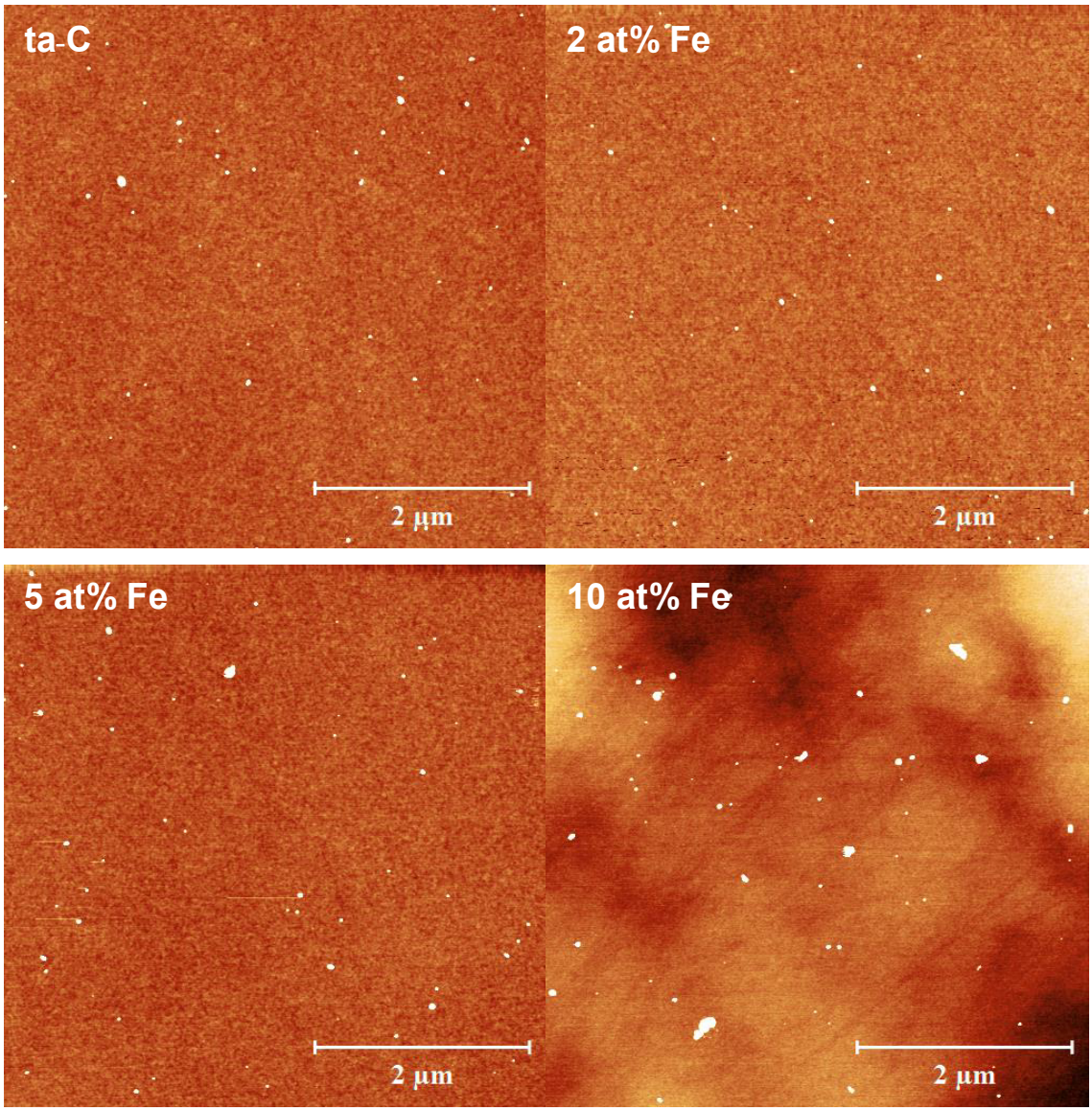

Figure B1. Additional 5x5 μm (512x512 resolution) AFM scans of the samples showing relative amounts of macroparticles and the surface topography. Also note the undulating surface structure of 10 at% Fe sample. Scale in all AFM height images is from 0 to 4 nm. However, most of the particles seen in white are considerable larger than 4 nm and therefore are out of range.

Figure B1 shows the relative amounts of macroparticles and the surface topography. Also, note the undulating surface structure of 10 at% Fe sample, which was also observed in other optical microscopes. The AFM scans in Figure B1 were used to select the 1x1 um areas for AFM scans in Figure 7. The smaller 1x1 μm areas were selected to calculate the surface roughness independent of the effect of macroparticles.

The relative amounts of macroparticles in Figure B1 appear comparable. Additionally, the amounts of macroparticles on each sample were found similar by mapping with an optical microscope and processing with ImageJ for particle count per area (data not shown). Furthermore, for meticulousness, it is imperative to identify whether particular macroparticles are of carbon (as expected in ta-C), or of iron. It should be firmly noted here, that this notion was purposefully disregarded parallel to iron crystallinity discussion due to limited time and resources. Further investigation is pending on this subject.

Appendix C. Crystallinity in Iron Calibration Series

Grazing incidence X-ray diffraction (GIXRD) was utilized to investigate the crystallinity of the iron deposition rate calibration samples (Fe 400p, Fe 600p, and Fe 800p). Figure C1 displays GIXRD omega/2-theta scans of the iron calibration series samples in the 2-theta range of 40-50 degrees. Backgrounds were adjusted by simple subtraction to enable comparison in the same background intensity range. Although not optimal, all samples were investigated with the same setup and incidence parameters to enable comparison. Incident vertical slit of 0.05 mm and incident horizontal slit 5 mm were used with a double Ge(220) monochromator at an omega angle of 0.5 deg. The effect of increased iron film thickness was revealed as an increase in the Fe {110} peak at around 44-45 degrees 2-theta [66].

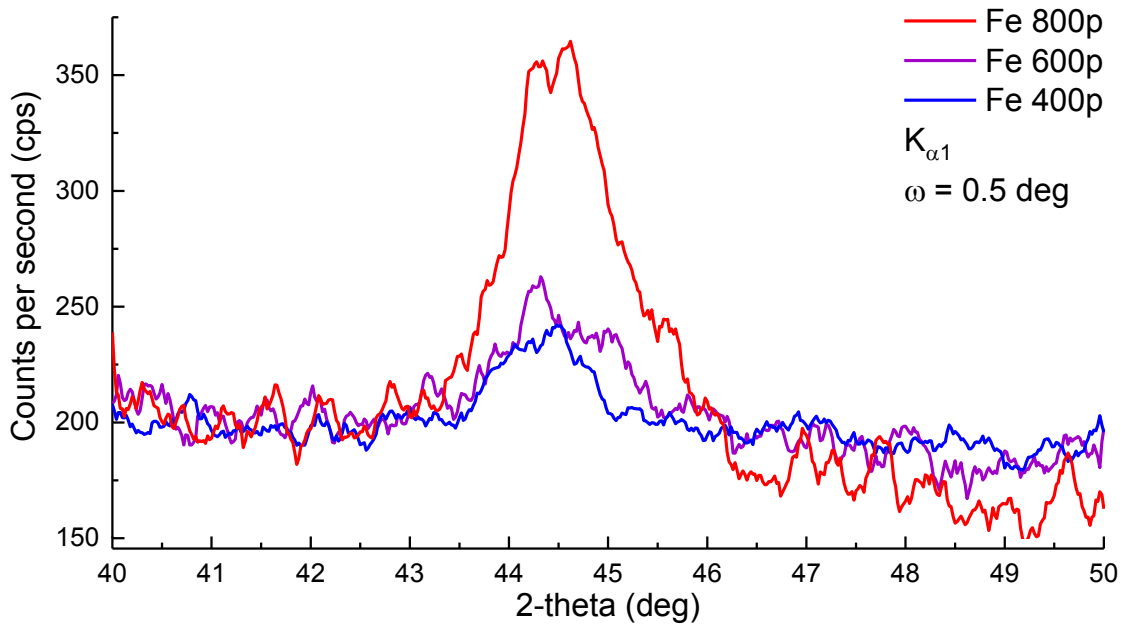

Figure C1. GIXRD omega/2-theta scans of the iron calibration series samples Fe 400p, Fe 600p, and Fe 800p in the 2-theta range of 40-50 degrees. All samples were investigated with the same setup and incidence parameters to enable comparison. Backgrounds were adjusted by simple subtraction to enable comparison.

Appendix D. Additional Electron Diffraction Diffractograms

Figures D1 exhibits the SAED diffractograms obtained for the Fe/ta-C samples of 2 and 5 at% Fe. There is a diffuse diffraction pattern visible, which might also be partially due to non-specular small angle scattering.

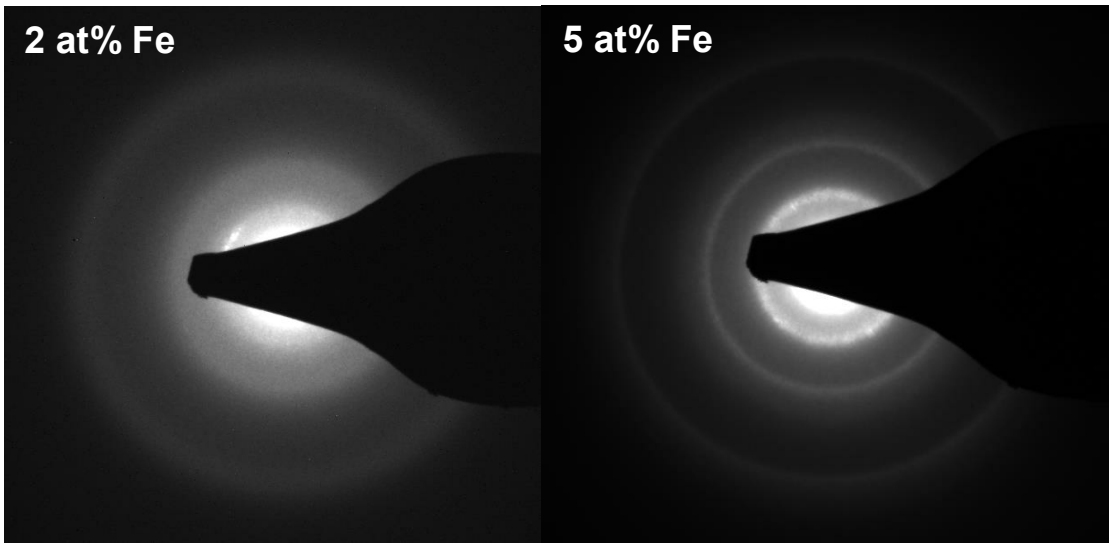

Figure D1. SAED patterns obtained for 2 and 5 at% Fe/ta-C. There are no distinct diffraction patterns apparent similar to the SAED in Figure 9.

Appendix E. Cyclic Voltammetry Peak Redox Currents

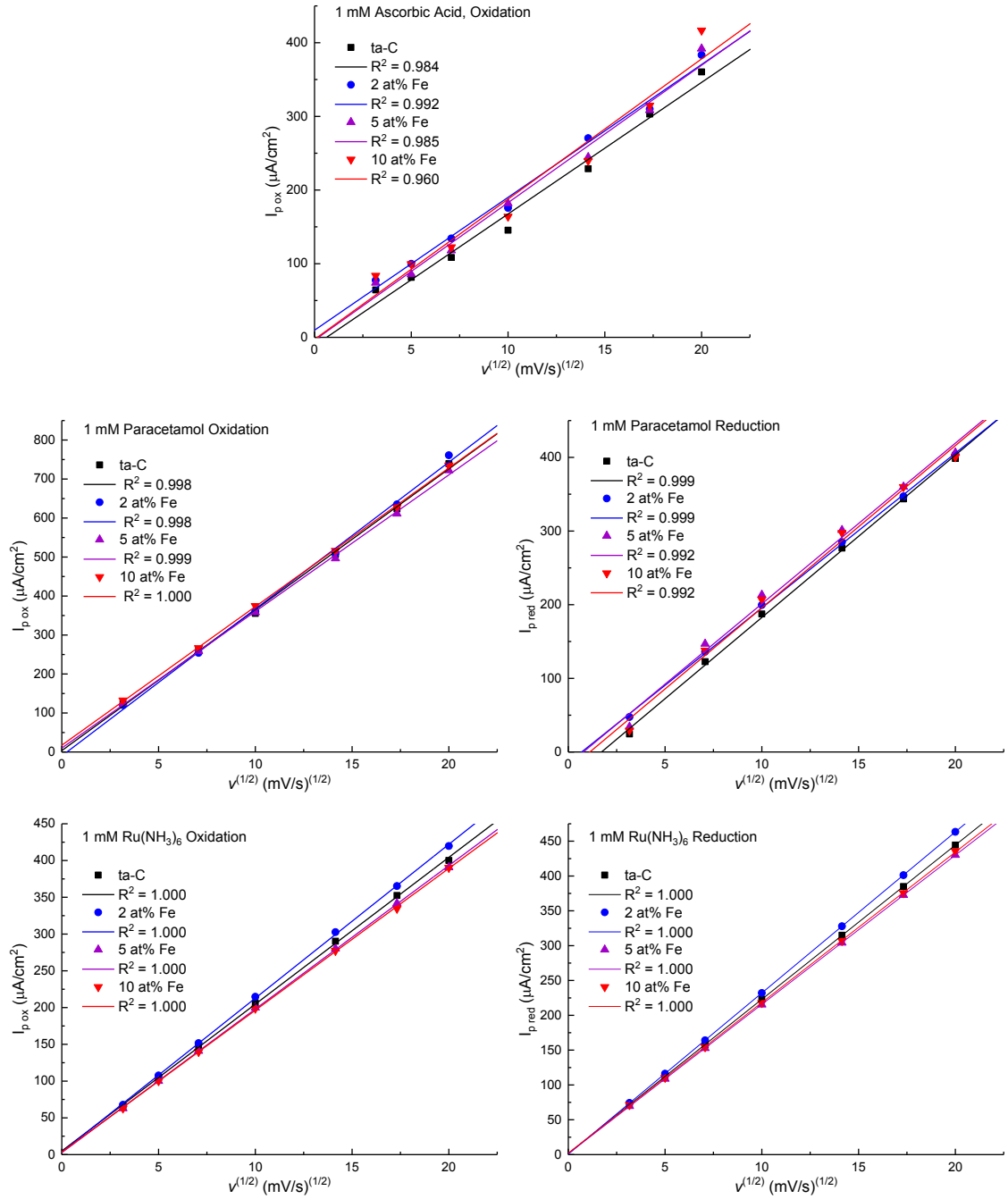

Figure E1. Linear correlations of oxidation and reduction peak currents (I_p) as functions of $\upsilon^{(1/2)}$ for ascorbic acid, paracetamol and $Ru(NH_3)_6$.